

ABSTRACT

Title of dissertation: STUDIES OF ATOMIC
 PROPERTIES OF FRANCIUM
 AND RUBIDIUM

Adrián Pérez Galván,
Doctor of Philosophy, 2009

Dissertation directed by: Professor Luis A. Orozco
 Department of Physics

High precision measurements of atomic properties are excellent probes for electroweak interaction studies at the lowest possible energy range. The extraction of standard model coupling constants relies on a unique combination of experimental measurements and theoretical atomic structure calculations. It is only through stringent comparison between experimental and theoretical values of atomic properties that a successful experiment can take place. Francium, with its heavy nucleus and alkali structure that makes it amenable to laser cooling and trapping, stands as an ideal test bed for such studies.

Our group has successfully created, trapped and cooled several isotopes of francium, the heaviest of the alkalis, and demonstrated that precision studies of atomic properties, such as the measurement of the $8S_{1/2}$ excited state lifetime of ^{210}Fr presented here, are feasible. Further work in our program of electroweak studies requires a better control of the electromagnetic environment observed by the sample of cold atoms as well as a lower background pressure (10^{-10} torr or better). We have

designed and adapted to our previous setup a new “science” vacuum chamber that fulfills these requirements and the transport system that will transfer the francium atoms to the new chamber.

We use this new experimental setup as well as a rubidium glass cell to perform precision studies of atomic and nuclear properties of rubidium. Spectroscopic studies of the most abundant isotopes of rubidium, ^{85}Rb and ^{87}Rb , are a vital component in our program. Performing measurements in rubidium allows us to do extensive and rigorous searches of systematics that can be later extrapolated to francium.

We present a precision lifetime measurement of the $5D_{3/2}$ state of ^{87}Rb and a measurement of hyperfine splittings of the $6S_{1/2}$ level of ^{87}Rb and ^{85}Rb . The quality of the data of the latter allows us to observe a hyperfine anomaly attributed to an isotopic difference of the magnetization distribution in the nucleus *i.e.* the Bohr-Weisskopf effect. The measurements we present in this work complement each other in exploring the behavior of the valence electron at different distances from the nucleus. In addition, they constitute excellent tests for the predictions of *ab initio* calculations using many body perturbation theory and bolster our confidence on the reliability of the experimental and theoretical tools needed for our work.

STUDIES OF ATOMIC
PROPERTIES OF FRANCIUM AND RUBIDIUM

by

Adrián Pérez Galván

Dissertation submitted to the Faculty of the Graduate School of the
University of Maryland, College Park in partial fulfillment
of the requirements for the degree of
Doctor of Philosophy
2009

Advisory Committee:
Professor Luis A. Orozco, Chair/Advisor
Professor Steven L. Rolston
Professor Carter R. Hall
Professor Elizabeth J. Beise
Professor Michael A. Coplan

© Copyright by
Adrián Pérez Galván
2009

Acknowledgments

Vulgarization of knowledge through the widespread distribution of printed material as well as virtual *i.e.* the web, has left little of the pleasure of struggling to acquire it. Granted, the possibility of having an almost infinite amount of information at your fingertips that enriches your everyday life is nothing to complain about. However, I have found that the urge to acquire more information as fast as possible has left us lacking something that I cannot quite define.

In this context, then, it is quite peculiar that the very antiquated tradition of communication of knowledge, an apprenticeship, has survived today in the form of the doctoral program. Under the tutelage of the advisor, the apprentice or student, is formed and deformed in the mysterious ways (in the case of physics) of the scientific method not unlike the sword-smith that shows his apprentice the precise amount of carbon to add to his iron to make the knife resistant or the painter that teaches the necessary techniques as well as the proper mixture of pigments to make the desired color. The main difference is that the material modeled and battle tested is the being of the student. Of course, just like in any other trade, the craft does not stop as one leaves the office or the laboratory and one finds, if things are being set down properly, that one confronts the outside, in the very specific case of the sciences, as a scientist.

I firmly believe this has been my case during the last five and a half years working under the direction of my advisor Luis A. Orozco. The work I am presenting in this thesis reflects the effort and time he and I have spent in the laboratory but

does not stand as his main achievement, which is, giving me the trade of the scientist. I have, willingly, acquired this enormous debt, have no idea how to repay it and hope that it will not be undone.

It is also my great pleasure to acknowledge the invaluable support of my parents without whom I could not have gone far.

I have met several people along the way, both in and outside the laboratory. Of all of them I want to acknowledge (due to space reasons) Eduardo Gomez, Fernando Galaz, and Elohim Becerra for their exchange of ideas and support, Gene Sprouse for his help during my stay at Stony Brook and the following years, Yanting Zhao for his help in the laboratory at University of Maryland, and my lab partner of the last few years and now senior student of the laboratory Dong Sheng. I want also to thank my very patient girlfriend Laura Kimes and acknowledge that hard is the life of the scientist but harder the life of the girlfriend of the scientist.

Table of Contents

List of Tables	vi
List of Figures	vii
1 The weak interaction in atomic physics and the measurement of the nuclear anapole moment	1
1.1 Introduction	1
1.2 Theoretical background	4
1.3 Measurement strategy	9
1.4 New experimental setup	11
2 Measurement of the hyperfine splitting of the 6s state of rubidium	23
2.1 Introduction	23
2.2 Theoretical background	24
2.2.1 Hyperfine interaction	24
2.2.2 <i>Ab initio</i> calculations	26
2.2.3 Hyperfine anomalies	28
2.2.4 Breit-Crawford-Rosenthal-Schawlow effect	29
2.2.5 Bohr-Weisskopf effect	32
2.2.6 Two-photon spectroscopy	35
2.3 Measurement of the hyperfine splitting	42
2.3.1 Apparatus	42
2.3.2 Method	45
2.3.3 Results and systematic effects	50
2.4 Comparison with theory	60
2.5 Conclusions	60
3 Measurements of lifetimes of excited states of francium and rubidium	66
3.1 Introduction	66
3.2 Theoretical background	67
3.3 Measurement of lifetimes of excited states	68
3.3.1 Time correlated single photon counting method	68
3.3.2 Experimental setup	70
3.3.2.1 8s state of francium	70
3.3.2.2 5D _{3/2} state of rubidium	77
3.4 Experimental results and systematics	80
3.4.1 8s state in francium	82
3.4.1.1 Systematics	82
3.4.2 5D _{3/2} state of rubidium	85
3.4.2.1 Systematics	87
3.5 Comparison with theory	87
3.6 Conclusions	89

4	Conclusions and outlook	91
A	Two-photon lock.	94
A.1	Introduction	94
A.2	Theoretical model	96
A.3	Apparatus and method	101
A.4	Conclusions	107
	Bibliography	110

List of Tables

1.1	Specifications of conflat flanges of science chamber.	17
1.2	Number of atoms at $T=150 \mu\text{K}$ that remain within the area defined by the inner radius of the differential pumping system ($r_0 = 0.5 \text{ cm}$). V_1 and V_2 correspond to calculations considering 20 m/s and 15 m/s as an initial velocity in the $-z$ direction, respectively. The subindex A and M denotes an analytical or a Montecarlo solution to the problem.	22
2.1	Values of ϵ_{BCRS} and corresponding nuclear radius for both rubidium isotopes.	31
2.2	Theoretical and experimental values of the nuclear dipole moment for rubidium.	34
2.3	Error budget for the hyperfine splitting measurement	58
2.4	Hyperfine splittings (ν_{HF}) and magnetic dipole constants for the $6S_{1/2}$ level.	60
2.5	SDpT and CCSD theoretical predictions calculated using <i>ab initio</i> MBPT from Ref. [34] and Ref. [35], respectively, and experimental magnetic dipole constants for the first $J=1/2$ levels in ^{85}Rb	63
2.6	Hyperfine anomaly differences $_{87}\delta_{85}$ for the first $J=1/2$ levels in rubidium.	65
3.1	Error budget of the measurement of the lifetime of the $8S_{1/2}$ state of francium.	83
3.2	Error budget of the measurement of the $5D_{3/2}$ state lifetime of rubidium.	88
3.3	Comparison of the measured lifetime of the $8S_{1/2}$ state of francium with <i>ab initio</i> calculations.	88
3.4	Comparison of the measured lifetime of the $5D_{3/2}$ state of rubidium with previous work and calculations.	89
4.1	Summary of spectroscopic measurements presented in this thesis. . .	93

List of Figures

1.1	Contributions to the spin-dependent PNC transition amplitude. . . .	6
1.2	Block diagram of new experimental setup.	12
1.3	xz plane view of science chamber.	13
1.4	yz plane view of science chamber.	14
1.5	xy plane view of science chamber.	15
1.6	Time sequence for transfer of atoms.	18
1.7	Atomic fluorescence in upper chamber during transfer sequence. . . .	20
1.8	Atomic fluorescence in science chamber during transfer sequence. . . .	21
2.1	Nuclear charge radius of Rb isotopes.	30
2.2	Energy levels of rubidium relevant for the measurement of the hyperfine splitting of the $6S_{1/2}$ state.	36
2.3	Energy levels of the five level theoretical model.	37
2.4	Numerical simulation of absorption of 795 nm laser as a function of 1.3 μ laser detuning.	39
2.5	Block diagram of experiment.	41
2.6	Experimental trace of the absorption of the 795 nm laser as a function of 1.3 μ m laser detuning.	43
2.7	Sideband crossing in ^{85}Rb	46
2.8	Decrease and increase of absorption of 795 nm laser as a function of 1.3 μ m laser due to optical pumping.	47
2.9	Sidebands of ^{87}Rb with fits to Lorentzian and Gaussian profiles. . . .	49
2.10	Numerical derivative of sidebands in ^{85}Rb	53
2.11	Zeeman plot of the $6S_{1/2}$ hyperfine separation in ^{85}Rb	55
2.12	Results of different runs of the magnetic dipole constants of the $6S_{1/2}$ state of ^{85}Rb	59

2.13	Comparison of experimental and theoretical values of the hyperfine splitting of the $6S_{1/2}$ state in ^{85}Rb	61
2.14	Comparison of experimental and theoretical values of the hyperfine splitting of the $6S_{1/2}$ state in ^{87}Rb	62
2.15	Hyperfine anomalies of first $J = 1/2$ levels of rubidium.	64
3.1	Typical time sequence in a correlated single photon counting experiment.	69
3.2	Plane view of the dry film coated cell and neutralizer mechanism. . .	71
3.3	Cross section of the dry film coated cell and neutralizer mechanism. .	72
3.4	Energy levels of francium relevant for the measurement of the lifetime of the $8S_{1/2}$ state of francium.	74
3.5	Block diagram of the experiment of the measurement of the lifetime of the $8S_{1/2}$ state of francium.	76
3.6	Energy levels of ^{87}Rb relevant for the measurement of the lifetime of the $5D_{3/2}$ state.	78
3.7	Experimental data of the decay of the $8s$ state of francium.	81
3.8	Experimental data of the decay of the $5D_{3/2}$ state.	86
A.1	Energy levels relevant for the locking of the 776 nm laser and theoretical model.	97
A.2	Numerical simulation of the absorption of the modulated pump laser.	100
A.3	Numerical simulation of the demodulated absorption of the pump laser as a function of the probe detuning.	102
A.4	Block diagram of the experiment.	103
A.5	DC component of the absorption of the 780 nm laser light as a function of the detuning of the 776 nm laser.	105
A.6	Experimental traces of the unmodulated absorption of the 780 nm laser as a function of the detuning of the 776 nm laser.	106
A.7	Fringe side transmission of the 776 nm laser light through a Fabry-Perot confocal cavity.	108

Chapter 1

The weak interaction in atomic physics and the measurement of the nuclear anapole moment

1.1 Introduction

Francium, the heaviest of the alkalis, is an ideal system to perform studies of the electroweak interaction at low energies [1, 2, 3]. Its alkali structure allows the confinement of a sample of cold francium atoms to a small region of space using standard techniques of laser cooling and trapping [4]. Once trapped, a plethora of tools to manipulate the inner and outer degrees of freedom of the atom can be employed. Theoretical calculations of the electronic wave function can be done with great accuracy which are vital for the extraction of parameters from experiment of the electroweak theory. How accurately a value can be extracted from experiment, it has been shown [5, 6], will ultimately depend on the quality of the theoretical calculations.

On the nuclear side, the heavy nucleus of the francium atom ($Z = 87$) makes the interactions between the electronic cloud and the nucleus more conspicuous than in lighter alkalis increasing the probability of observing the minutiae of the rich interplay between these two systems such as parity violating effects. The observation of these manifestations of the weak force in a chain of francium isotopes is the long

term goal of the Francium Parity Non-Conservation (FrPNC) collaboration.

The measurement of parity non-conserving (PNC) effects is the final keystone of a long experimental program that involves the creation of francium (it does not have any stable isotopes), the development of experimental techniques, design and test of equipment, and precision spectroscopic studies of atomic and nuclear properties. The first step was taken in 1995 when the group managed to create and trap one thousand francium atoms in a magneto-optical trap (MOT) [7]. Further work on the creation and trapping efficiency pushed the number of atoms upward to the hundred thousands [8]. The increase in the number of atoms trapped allowed for higher precision and accuracy in the spectroscopic studies that followed. The group devoted several years to the understanding of the electronic structure through spectroscopy of francium [9, 10, 11, 12, 13, 14].

Our experimental program has been followed closely by an equally stringent theoretical program of calculation of atomic properties performed by several groups using many-body perturbation theory (MBPT) (see Chapters 2 and 3). Extraction of weak interaction parameters requires expectation values of certain matrix elements [28] that cannot be extracted from experiment. The precision with which these parameters are determined is strongly dependent on the precision with which the valence electron wavefunction is known. It is of the utmost importance for the theory to reach a precision of less than a percent since previous work in other atomic systems [5, 6] has shown that theoretical input limits the precision of the parameters extracted from the experiment.

In this thesis we present a set of measurements of atomic properties in both

rubidium and francium atoms that bolster our confidence on the theoretical and experimental techniques vital for observation of a parity violating effects in the scattering rate of light by different francium isotopes. Spectroscopic studies of the most abundant isotopes of rubidium, ^{85}Rb and ^{87}Rb , are a vital component in our program. Performing measurements in rubidium allows us to do extensive and rigorous searches of systematics that can be later extrapolated to francium. Comparison of experimental and theoretical atomic properties of rubidium presents an excellent opportunity to gauge the accuracy of the calculations in another atomic system. We also present in this thesis the work done in the design of the new experimental setup that will be added to the high efficiency trapping setup used at the Nuclear Structure Laboratory at Stony Brook and will ultimately be transported to TRIUMF in Vancouver, Canada.

The thesis is arranged as follows. Chapter 1 describes the new experimental setup as well as the transportation system that will guide the atoms to this new setup. A brief introduction of the theory behind atomic parity non-conservation experiments as well as a quick overview of the experimental scheme that will be used is also included in this section. A thorough study of the proposed experiment can be found in Ref. [2]. Chapter 2 presents the measurement of the hyperfine splitting of the $6S_{1/2}$ level in ^{87}Rb and ^{85}Rb and the extraction of a hyperfine anomaly from these two measurements. Chapter 3 concludes the thesis with two measurements of lifetimes of excited states in two different atoms: the lifetimes of the $5D_{3/2}$ state of ^{87}Rb and the $8S_{1/2}$ state of ^{210}Fr . Chapter 4 has the overall conclusions and an outlook of things to come. At the end of the thesis an Appendix presents the

two-photon two-color lock used during the measurement of the lifetimes of the $5D_{3/2}$ state.

1.2 Theoretical background

The Hamiltonian of an atomic system no longer commutes with the parity operator due to the exchange of weak bosons between nucleons [15]. This results in a term in the total Hamiltonian that is dependent on the handedness of the coordinate system observed by the atom. The nature of the coupling between the hadronic and electronic currents allows the classification of the interaction in two types: nuclear spin-dependent and nuclear spin-independent. In the spin-independent interaction the electron plays the role of the axial current and is usually the larger of the two; its behavior depends on the collective behavior of all the nucleons. The spin-dependent interaction has the electron as the vector current with the configuration of the valence nucleons determining the characteristics of the interaction instead of the whole nucleus. This makes the nuclear spin-independent interaction strongly dependent on nuclear models. Both of these interactions share some common characteristics such as a close range behavior and dependence of the size of the effect on some power of the nuclear charge. The FrPNC collaboration interest lies in studies, in different isotopes, of the spin-dependent interaction [2].

The parity-violating contribution to the atomic Hamiltonian, in the limit of an infinitely heavy nucleon, without radiative corrections, is given by [16]:

$$H_{PNC} = \frac{G}{\sqrt{2}}(\kappa_{1i}\gamma_5 - \kappa_{nsd,i}\vec{\sigma}_n \cdot \vec{\alpha})\delta(\vec{r}), \quad (1.1)$$

where $G = 10^{-5}/m_p^2$ is the Fermi constant, m_p is the mass of the proton, γ_5 and $\vec{\alpha}$ are Dirac matrices, $\vec{\sigma}_n$ are Pauli matrices, and κ_{1i} and $\kappa_{nsd,i}$ with $i = n, p$ for a neutron and a proton are constants of the interactions and nsd stands for nuclear spin-dependent. The Dirac delta emphasizes the close range interaction between the fermionic and hadronic currents coming from the large mass of the weak neutral boson. The first of the terms of Eq. 1.1 is the spin-independent contribution and is proportional to the weak charge Q_W . The weak charge is $Q_W = -N + Z(1 - 4\sin^2\theta_W)$ which is almost equal to $-N$ ($\sin^2\theta_W \approx 0.23$). In order to extract the weak charge from an experiment it becomes necessary to calculate the matrix element of γ_5 which is where the uncertainty of the theoretical calculations appears. The non-relativistic approximation of Eq. 1.1 presents a more transparent expression and helps develop a physical intuition of the process. For very light atoms (where $Z\alpha \ll 1$), the nuclear spin-dependent contribution can be expressed, to lowest order in the velocity of the electron \vec{p}/m , as the inner product of the nuclear or electronic spin with the velocity [16]. This product ($\vec{p} \cdot \vec{\sigma}$) corresponds to the simplest pseudoscalar that violates parity.

At tree level $\kappa_{nsd,i} = \kappa_{2i}$ and the constants of the interaction are given by

$$\begin{aligned} \kappa_{1p} &= \frac{1}{2}(1 - 4\sin^2\theta_W), \quad \kappa_{1n} = -\frac{1}{2}, \\ \kappa_{2p} &= -\kappa_{2n} \equiv \kappa_2 = -\frac{1}{2}(1 - 4\sin^2\theta_W)\eta, \end{aligned}$$

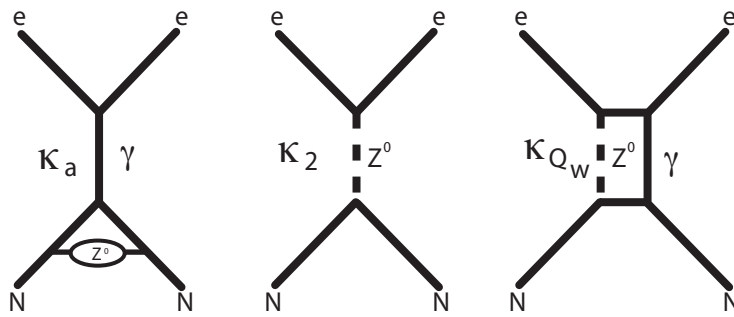


Figure 1.1: Contributions to Eq. 1.3 arising from the exchange of a Z_0 boson in the nuclear spin dependent Hamiltonian. The diagrams appear beside the coupling constant they describe.

with $\eta = 5/4$. κ_{1i} (κ_{2i}) represents the coupling between nucleon and electron currents when the electron (nucleon) is the axial vector. It is necessary to add the contribution from each of the nucleons of the atom. To carry this out it is convenient to consider a single valence nucleon in the nuclear shell model approximation with an unpaired spin. This yields, for the nuclear spin-dependent contribution [17]:

$$H_{PNC}^{nsd} = \frac{G}{\sqrt{2}} \frac{K \vec{I} \cdot \vec{\alpha}}{I(I+1)} \kappa_{nsd} \delta(\vec{r}), \quad (1.2)$$

where $K = (I + 1/2)(-1)^{(I+1/2-l)}$, where l is the nucleon orbital angular momentum, and \vec{I} is the nuclear spin. The terms proportional to the anomalous magnetic moment of the nucleons and the electrons have been neglected. The interaction constant is given by [17]

$$\kappa_{nsd} = \kappa_a - \frac{K - 1/2}{K} \kappa_2 + \frac{I + 1}{K} \kappa_{QW}, \quad (1.3)$$

where $\kappa_2 \approx -0.05$. The three terms shown can be traced to different ways in which the weakly interacting vector boson Z_0 appears in the Feynman diagrams (see Fig 1.1). The first and last term represent corrections to the interaction. The first and biggest contribution, the nuclear anapole moment (κ_a) corresponds to vertex corrections in a heavy atom due to weak hadronic interactions on the nuclear side of the electromagnetic interaction coupled to the electron through a virtual photon where κ_a is the effective constant of the moment. The second one takes the direct effect of a Z_0 exchange between the electron vector current and the nuclear axial current. The last and smallest one is the simultaneous exchange of a Z_0 and a

photon modifying the hyperfine interaction. Flambaum and Murray showed that both κ_{QW} and κ_a scale as $A^{2/3}$ where A is the atomic mass number. The anapole moment is the dominant contribution to the interaction in heavy atoms.

The anapole moment is defined by [17]

$$\vec{a} \equiv -\pi \int d^3r r^2 \vec{J}(\vec{r}), \quad (1.4)$$

where \vec{J} is the nuclear current density. Flambaum *et al.* [18] estimate the anapole moment of a single valence nucleon to be (as in the odd isotopes of francium)

$$\vec{a} = \frac{1}{e} \frac{G}{\sqrt{2}} \frac{K \vec{j}}{j(j+1)} \kappa_{a,i} = C^{an} \vec{j}, \quad (1.5)$$

where \vec{j} is the nucleon angular momentum and e is the charge of the electron. For the case of a single valence nucleon these values are the nuclear ones ($\vec{j} \rightarrow \vec{I}$).

The anapole moment induces a small mixing of electronic states of opposite parity. The effect on the ground state hyperfine levels according to first order non-relativistic perturbation theory is [17]

$$|\overline{sFm}\rangle = |sFm\rangle + \sum_{F'm'} \frac{\langle pF'm' | H_a | sFm \rangle}{E_p - E_s} |pF'm'\rangle \quad (1.6)$$

where E_p and E_s are the energies of the p and s states, respectively, F is the total angular momentum of the atom, m is the magnetic quantum number, and

$$H_a = |e| \vec{\alpha} \cdot \vec{a} \delta(\vec{r}) \quad (1.7)$$

is the nuclear anapole moment Hamiltonian from Eq. 1.2. In practice, the mixing is measured through an $E1$ transition amplitude A_{E1} induced by the anapole moment

between two hyperfine levels [2]

$$A_{E1} = \langle sFm | -e\vec{E} \cdot \vec{r} | s(F+1)m' \rangle \propto \kappa_a \times E, \quad (1.8)$$

where E is the magnitude of the electric field driving the transition.

1.3 Measurement strategy

A high efficiency magneto-optical trap (MOT) for francium atoms has been demonstrated by our group in a dry film coated glass cell online with an accelerator [8]. It is necessary, however, to transfer the atomic sample to another location where the electromagnetic environment as well as the background pressure (10^{-10} torr or better) are better controlled (see Figs. 1.3, 1.4, and 1.5 in next section), *i.e.* a “science” chamber. Once in this science chamber, the atoms will be loaded into a dipole trap located at the electric field antinode of a standing wave of a microwave Fabry-Perot cavity. Laser beams will polarize the atoms into a single Zeeman sublevel of the lowest hyperfine ground state, and a Raman pulse of amplitude A_R and duration t_R will prepare a coherent superposition of the hyperfine ground levels (see Chapter 3 for a typical diagram of the energy levels). Simultaneously, we will drive the $E1$ parity-forbidden transition of amplitude A_{E1} with the cavity microwave field, and measure the population in the upper ground hyperfine level normalized by the total number of atoms N using a cycling transition [2]. The number of atoms transferred at the end of each sequence will be

$$\Xi_{\pm} = N|c_e|^2 = N \sin^2\left(\frac{(A_R \pm A_{E1})t_R}{2\hbar}\right), \quad (1.9)$$

where c_e is the upper hyperfine level population. The sign depends on the handedness of the coordinate system defined by the external electric and magnetic fields. The signal for the measurement,

$$\begin{aligned} S = \Xi_+ - \Xi_- &= N \sin\left(\frac{A_R t_R}{\hbar}\right) \sin\left(\frac{A_{E1} t_R}{\hbar}\right) \\ &\approx N \sin\left(\frac{A_R t_R}{\hbar}\right) \left(\frac{A_{E1} t_R}{\hbar}\right), \end{aligned}$$

will be the difference between populations in the upper hyperfine level for both handedness. The last step assumes a small parity violating transition amplitude.

The magnitude of the signal from Eq. 1.9 reaches a maximum for a Raman transition amplitude of $A_R = (2n + 1)\pi/2$ with $t_R = 1$ s. The measurement of the upper hyperfine state population collapses the state of each atom into one of the two hyperfine ground state levels. The collapse distributes the atoms binomially between the two hyperfine levels and leads to an uncertainty in the population called projection noise N_P [19]. The projection noise is given by

$$N_P = \sqrt{N|c_e|^2(1 - |c_e|^2)}. \quad (1.10)$$

The projection noise vanishes when all the atoms are in one of the hyperfine levels, but in those cases the noise is dominated by other sources, such as the photon shot noise. The signal-to-noise ratio for a projection-noise limited measurement is

$$\frac{S}{N_P} = 2 \frac{A_{E1} t_R}{\hbar} \sqrt{N}. \quad (1.11)$$

We expect to obtain in a single shot, with typical experimental parameters [2] and $t_R = 1$ with 10^6 atoms, an uncertainty of 5%.

1.4 New experimental setup

The electromagnetic and vacuum environment present inside our dry film glass cell does not satisfy the stringent requirements necessary for the correct performance of the proposed measurements. The atomic sample needs to be transported to another region where a better control of the fields that define the handedness of the coordinate system observed by the atoms can be provided. We have designed a transport system and a new chamber where the experiment will take place following the guidelines set by our experimental scheme.

Figure 1.2 shows a diagram of the vacuum components that form the new experimental setup, the inset shows the transportation system. Our setup currently resides at the University of Maryland for testing and optimization before being sent to TRIUMF in Vancouver, Canada where we will be provided with a high intensity beam of francium atoms.

Figures 1.3, 1.4, and 1.5 show the projections on each of the planes of the science chamber. The number and position of the flanges follow the guidelines set by our experimental scheme. Table 1.1 has the description of each of the numbered conflat flanges and the suggested use of each for the experimental scheme [20]. The “free” ports will be used for light collection systems.

The setup has been tested with rubidium atoms. The science chamber is connected to a mock-up version of the glass cell used to trap francium from Kimball Physics (model MCF450-SC60008) through the transportation system. The science chamber was custom made by Kimball Physics using the designs shown in Figs. 1.3,

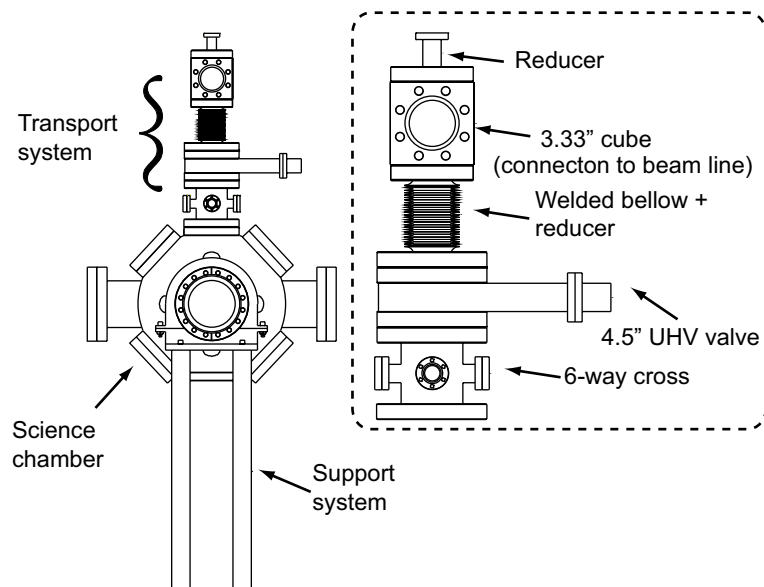


Figure 1.2: New experimental setup. The inset shows the transportation system. The dry film coated glass cell is not shown.

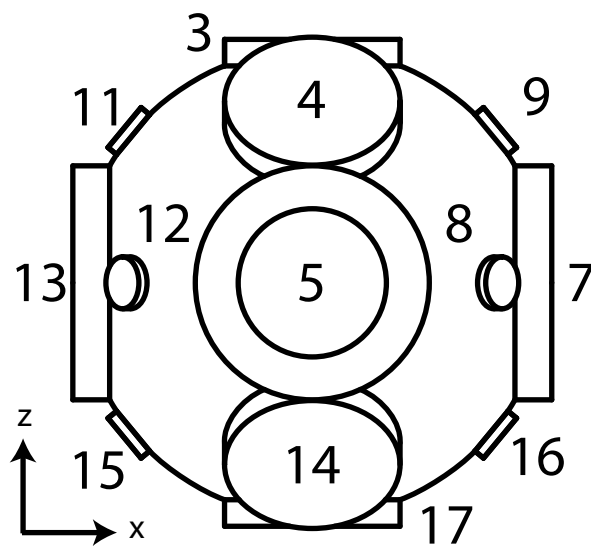


Figure 1.3: xz plane view of the science chamber. See Table 1.1 for the specifications of the numbered conflat flanges.

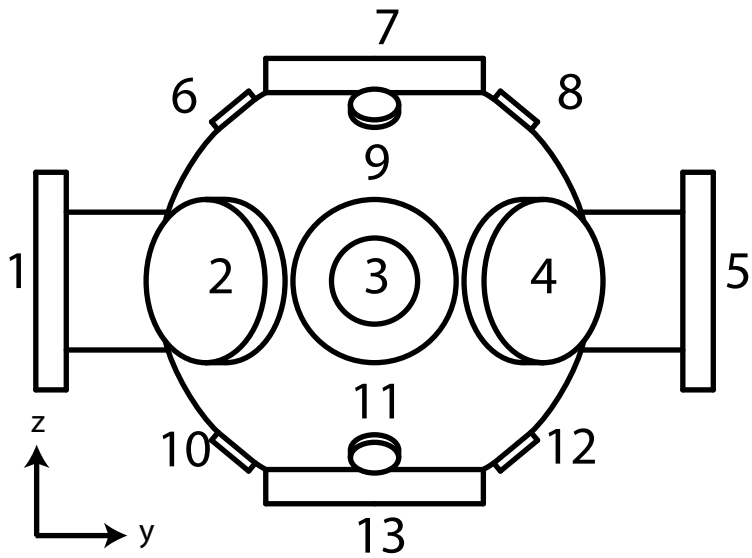


Figure 1.4: yz plane view of the science chamber. See Table 1.1 for the specifications of the numbered conflat flanges.

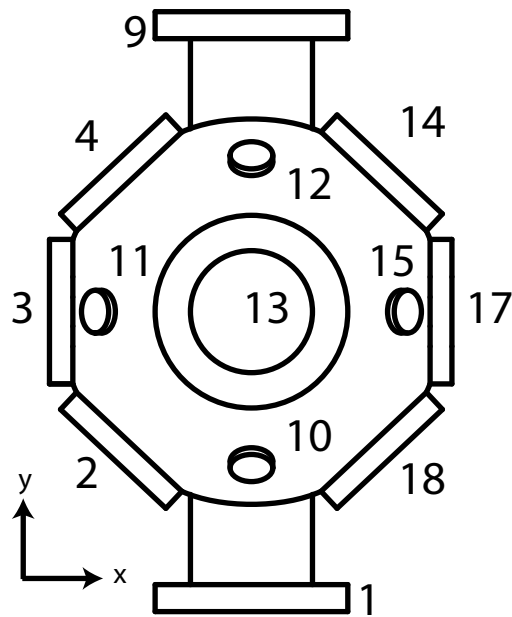


Figure 1.5: xy plane view of the science chamber. See Table 1.1 for the specifications of the numbered conflat flanges.

1.4, and 1.5. An OFHC copper pipe sits inside the bellows (see Fig. 1.2) that works as a differential pumping system that keeps the pressure in the science chamber (better than 10^{-10} torr) two orders of magnitude lower than in the upper chamber. The bellows in the transportation system mechanically uncouples the upper and the lower chambers. The pipe that works as the differential pumping system has an inner radius of 0.5 cm, a length of 12.7 cm, and a conductance of 1.1 L/s. The double vacuum chamber is continuously pumped by two (owned by Stony Brook University) ion-pumps from Varian with a pumping speed of 150 L/s (lower chamber) and 30 L/s (upper chamber).

Inside each chamber we have rubidium dispensers from SAES getters that provide rubidium atoms to load our MOTs (see Chapter 3 for a typical experimental setup for trapping atoms). The viewports of the upper chamber have been dry film coated. We have observed the fluorescence in the trapping region in both chambers using CCD cameras with Computar 10X lenses as light collection systems. The fluorescence allows us to estimate the number and the temperature of the atoms in the traps. Working with similar clouds in rubidium as those expected in francium (half a million atoms), we measured a temperature of around $150 \mu\text{K}$ using standard time-of-flight techniques.

We have transferred ^{87}Rb atoms from the top chamber to the science chamber with an efficiency of more than 50%. A laser pulse with a duration of 2 ms and a DC power of 0.5 mW transfers momentum to the atoms effectively pushing them downward out of the trapping region. This “push” laser beam is linearly polarized and on resonance with the $5S_{1/2}, F = 3 \rightarrow 5P_{3/2}, F = 4$ atomic transition. Just as

Table 1.1: Specifications of conflat flanges of science chamber.

Flange Number	Description	Use
1	6" flange, through holes	Microwave cavity
2	4.5" flange, tapped holes	MOT beam
3	4.5" flange, tapped holes	Atom input
4	4.5" flange, tapped holes	MOT beam
5	6" flange, through holes	Microwave cavity
6	1.33" flange, tapped holes	Raman beam
7	6" flange, tapped holes	MOT beam
8	1.33" flange, tapped holes	Dipole trap
9	1.33" flange, tapped holes	Free
10	1.33" flange, tapped holes	Free
11	1.33" flange, tapped holes	Free
12	1.33" flange, tapped holes	Free
13	6" flange, tapped holes	MOT beam
14	4.5" flange, tapped holes	MOT beam
15	1.33" flange, tapped holes	Free
16	1.33" flange, tapped holes	Free
17	4.5" flange, tapped holes	Free
18	4.5" flange, tapped holes	MOT beam

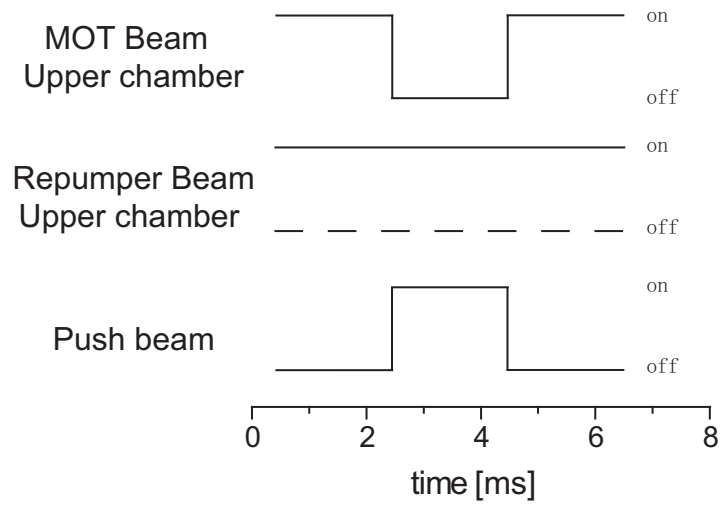


Figure 1.6: Time sequence for the transfer of atoms.

the push laser displaces the atoms, we turn off the MOT beams while leaving the repumper beam on. See Fig. 1.6 for the time sequence.

Figures 1.7 and 1.8 show the fluorescence of the rubidium atoms in both trapping chambers as a function of time. Fig. 1.7 is the fluorescence from the top chamber. A sudden decrease in the fluorescence marks when the pushing laser “kicks” the atoms downward. Almost simultaneously, the fluorescence of the science chamber (Fig. 1.8) increases: the atoms have been transferred (a 70 cm long path) to the center of the science chamber.

We calculate the number of atoms inside a radius $r_0 = 0.5$ cm (inner radius of the differential pumping system) as a function of time using two different procedures to simulate the transfer process and understand better our losses. In both of them we model the atomic sample as a non-interacting gas that is randomly distributed in a sphere with a radius of $100 \mu\text{m}$ (estimated radius of the MOT) and with a temperature $T = 150 \mu\text{K}$. After the push beam interacts with it, the atoms acquire a velocity V_0 in the $-z$ direction. The transverse velocity still obeys a Maxwell distribution. The first calculation consists of a Montecarlo simulation of the system, the second one is an analytical solution to the problem. Both of these approaches give results that are in very good agreement with each other (see Table 1.2) and are in close agreement with the experimental result. The initial velocities employed in the calculation are consistent with previous measurements of pushing velocities [8]. However, further work is still necessary to try to maximize the efficiency. Possible issues that might be limiting our current values could be optical pumping to the other hyperfine ground state, temperature of the sample and deflection of the atoms

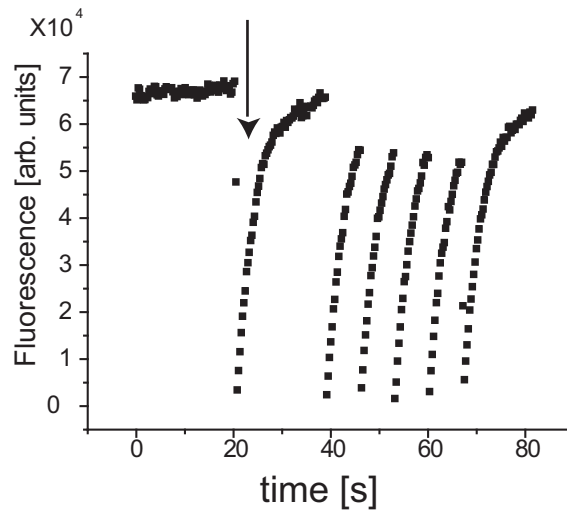


Figure 1.7: Atomic fluorescence in upper chamber as a function of time. The arrow shows the instant when the push beam displaces the atoms for the first time towards the science chamber. The increase of fluorescence is due to reloading of the MOT from the rubidium vapour provided by the getters. The difference in timing with Fig. 1.8 is due to the CCD cameras being activated at different times.

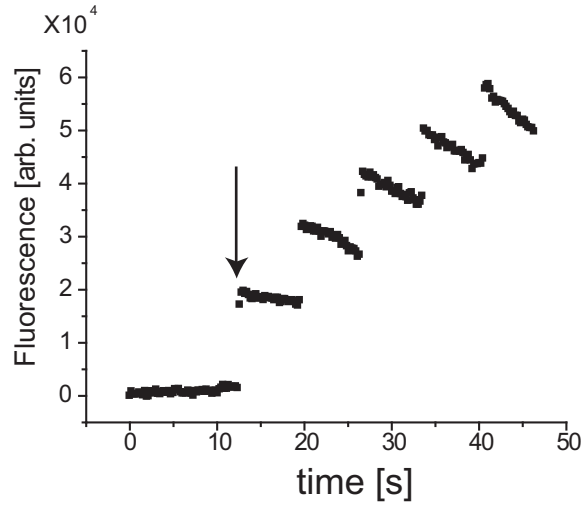


Figure 1.8: Atomic fluorescence in science chamber as a function of time. The arrow shows the instant when the atoms are recaptured in the science chamber after being pushed by the laser beam for the first time. Each subsequent increase of fluorescence corresponds to a successful transfer of rubidium atoms. The observed losses are due most probably to collisions with background gas. The difference in timing with Fig. 1.7 is due to the CCD cameras being activated at different times.

Table 1.2: Number of atoms at $T=150 \mu\text{K}$ that remain within the area defined by the inner radius of the differential pumping system ($r_0 = 0.5 \text{ cm}$). V_1 and V_2 correspond to calculations considering 20 m/s and 15 m/s as an initial velocity in the $-z$ direction, respectively. The subindex A and M denotes an analytical or a Montecarlo solution to the problem.

Falling distance [in]	$\%_{A}^{V_1}$	$\%_{A}^{V_1}$	$\%_{MC}^{V_2}$	$\%_{MC}^{V_0}$
3.2	100	100	100	100
6.9	99.99	100	99.8	100
8.6	99.94	99.9	98.5	98.7
12.7	96.7	95.8	85.5	85.4
17.0	85.0	84.7	65.9	66.5
25.2	58	59.2	39.1	37

by other laser beams [21] .

Chapter 2

Measurement of the hyperfine splitting of the $6s$ state of rubidium

2.1 Introduction

High precision measurements of hyperfine splittings are excellent testbeds for studies of the interaction between the atomic cloud and the nucleus [11, 22, 23, 24, 25, 26, 27]. Since the probability of the electron being inside the nucleus is nonzero, the electron becomes an excellent probe to explore fine details of interaction between them such as changes in nuclear matter distribution between isotopes. In addition, hyperfine splitting measurements represent ideal benchmarks for the *ab initio* calculations of the electronic wave function at distances close to the nucleus.

Measurements of hyperfine splittings are also important for studies of atomic parity non-conservation. Experiments of atomic PNC rely heavily on high precision calculations (better than 1% error) of operator expectation values to extract from the experimental data information on the weak interaction [28, 29, 30]. In the case of cesium, the value of the weak charge extracted from the experiment and the theory has yielded excellent agreement with the standard model [5, 31].

This chapter presents the measurement of the hyperfine splitting of the $6S_{1/2}$ level in ^{85}Rb and ^{87}Rb . The quality of the data allows us to extract, with the values of the gyromagnetic factors of both isotopes, an isotopic difference in the electronic wave function evaluated at the nucleus *i.e.* a hyperfine anomaly. The difference is in

excellent agreement with the one extracted from the ground state. Our experimental results are also in excellent agreement with theoretical prediction of MBPT of the hyperfine splittings.

This chapter starts with a brief introduction followed by the theoretical background in Section 2.2. Section 2.3 explains the experimental setup and method to measure the separation. This section also contains the experimental results and the results of the search of probable systematics. Section 2.4 compares our results with theory and Section 2.5 has the conclusions.

2.2 Theoretical background

2.2.1 Hyperfine interaction

The hyperfine interaction is accounted for by the interplay between the electromagnetic fields generated by the atomic cloud and the nuclear moments. Two types of nucleus-electron interactions, though, suffice to account for the interaction in most atoms. The largest of the contributions comes from the nuclear magnetic dipole coupling to the magnetic field created by the electrons at the nucleus. The second one arises from the interaction between the nuclear electric quadrupole and the gradient of the electric field generated by the electrons at the nucleus. The latter vanishes for spherically symmetric charge distributions ($J, I = 1/2$). The hyperfine energy shift E_{HF} for these levels is [32]:

$$E_{HF} = \frac{A}{2}(F(F+1) - I(I+1) - J(J+1)), \quad (2.1)$$

where F is the total angular momentum, I is the nuclear spin and A is the magnetic dipole interaction constant. The derivation of A for a hydrogen-like atom by Fermi and Segrè assumes a point nuclear magnetic dipole [33]

$$A_{point} = \frac{16\pi}{3} \frac{\mu_0}{4\pi\hbar} g_I \mu_N \mu_B |\psi(0)|^2, \quad (2.2)$$

where $\psi(0)$ is the electronic wave function evaluated at the nucleus, μ_B is the Bohr magneton, μ_N is the nuclear magneton and g_I is the nuclear gyromagnetic factor.

Under an external magnetic field, the atom acquires an extra potential energy coming from the alignment of the nuclear magnetic dipole with this field. For small values of the field ($g_F \mu_B B / E_{HF} \ll 1$) F is a good quantum number and the energy of the system is given by

$$E_{HF}(B) = E_{HF}(0) + g_F \mu_B m_F B, \quad (2.3)$$

where g_F is the total g-factor, m_F is the magnetic quantum number, B is the magnetic field and $E_{HF}(0)$ is the value of the energy at zero magnetic field. In this regime of small splittings compared to $E_{HF}(0)$, g_F is given by:

$$g_F = g_J \frac{F(F+1) + J(J+1) - I(I+1)}{2F(F+1)} - g_I \frac{F(F+1) + I(I+1) - J(J+1)}{2F(F+1)},$$

where g_J is the electronic g-factor.

2.2.2 *Ab initio* calculations

A thorough study of the hyperfine interaction must approach the problem from a relativistic standpoint which further complicates the problem in a multi-electron atom. In recent years relativistic many-body perturbation theory (MBPT) has shown itself to be a powerful and systematic way of extracting, from the high quality wave functions that it generates, precise atomic properties such as hyperfine splittings [34, 35].

The full method is outlined in Refs. [36, 37] and references therein. Briefly, the method, applied to alkali atoms, consists of evaluating a no-pair relativistic Hamiltonian with Coulomb interactions with a frozen core wave function of a one-valence electron atom. The Hamiltonian includes projection operators to positive energy states of the Dirac Hamiltonian. Their presence gives normalizable, bound state solutions. The wave function contains single and double excitations to all orders; these correspond to wave functions useful for calculating energy levels and transition matrix elements. In order to calculate accurate hyperfine constants a set of triple excitations has to be added. The evaluation of the wave function yields coupled equations that are solved iteratively for the excitation coefficients which are then used to obtain atomic properties. Predictions of the theory when the triple excitations are added are labeled single-double partial triple (SDpT) [34].

The increase in experimental precision in measurements of hyperfine splittings and the disagreement between theory and experiment of values of hyperfine splittings of d states has motivated theorist to include nonlinear coupled-cluster terms.

The disagreement stresses the importance of correlations between the electrons in higher excited states. The inclusion of all valence and core nonlinear coupled-cluster corrections to the once and twice excited equations allows to take into account the correlation effects with the predictions labeled coupled-cluster single-double (CCSD) [35].

The calculations of the hyperfine constants in the SDpT theory are corrected for the finite size of the nuclear magnetic moment up to zeroth order only due to their small size in the lighter alkalis (Na, K, Rb). In cesium and francium the correction becomes more important and is included to all orders. The calculation ignores isotopic changes of the magnetization distribution and it is modeled as a uniformly magnetized sphere for all the atoms. The magnetization radius is equal to the charge radius and the neutron skin contribution is ignored ¹. The CCSD theory considers the nuclear magnetization density as a Fermi distribution with half-density radius c and 90% - 10% falloff thickness $t=2.3$ fm [35].

¹Knowledge of the neutron skin ΔR_{np} , defined as the difference between the *rms* radii R_n and R_p of neutron and proton distributions, becomes important in calculations of parity violating amplitudes. The induced theoretical uncertainty ΔR_{np} induced an error that was of the same order of magnitude as the experimental error in the cesium work [5]. New calculations by Brown *et al.* show that the effect is better understood and place an upper correction to the parity violating amplitude in francium of 0.6% [38].

2.2.3 Hyperfine anomalies

The atomic electron sees the nucleus, most of the time, as a structureless entity with a single relevant parameter, its charge Z . We should expect, hence, the electronic wave functions of different isotopes, to a very good approximation, to be the same. It follows then, using Eq. 2.2 that the ratios of electronic wavefunctions, for the most abundant isotopes of rubidium, should be the same

$$\frac{A_{point}^{87}}{A_{point}^{85}} = \frac{g_I^{87}}{g_I^{85}}, \quad (2.4)$$

where the superindex denotes the atomic number of the isotope.

However, high precision experiments show differences or anomalies from this description. The nucleus is an extended structured intetity with specific finite magnetization and electric charge distributions for each isotope. We can express deviations from the point interaction by writing the magnetic dipole constant of an extended nucleus A_{ext} as a small correction to A_{point} [33]

$$A_{ext} = A_{point} f_R (1 + \epsilon_{BCRS}) (1 + \epsilon_{BW}), \quad (2.5)$$

where f_R represents the relativistic correction. The last two terms in parenthesis modify the hyperfine interaction to account for an extended nucleus. The Breit-Crawford-Rosenthal-Schawlow (BCRS) correction [39, 40, 41], the largest of the two, modifies the electronic wave function inside the nucleus as a function of the specific details of the nuclear charge distribution. The second one, the Bohr-Weisskopf (BW)

correction [42], describes the influence on the hyperfine interaction of the finite space distribution of the nuclear magnetization.

Up till now, extraction of ϵ_{BCRS} and ϵ_{BW} from experimental values has not been possible due to limits on the theoretical precision. However, the anomalies can still be observed from the measurements of the magnetic dipole constants in different isotopes and the values of the g -factors [43, 44]. Deviations from Eq. 2.4 are expressed in terms of the hyperfine anomaly difference ${}_{87}\delta_{85}$:

$$\frac{A^{87}g_I^{85}}{A^{85}g_I^{87}} \cong 1 + {}_{87}\delta_{85}, \quad (2.6)$$

with ${}_{87}\delta_{85} = \epsilon_{BW}^{87} - \epsilon_{BW}^{85} + \epsilon_{BCRS}^{87} - \epsilon_{BCRS}^{85}$. A ${}_{87}\delta_{85} \neq 0$ indicates the presence of a hyperfine anomaly.

2.2.4 Breit-Crawford-Rosenthal-Schawlow effect

The interaction between an electron and an atomic nucleus is precisely described by the Coulomb potential when both of them are far away from each other, no matter whether the nucleus is a point or an extended source. For interactions that require the nucleus and the electron to be very close to each other, an $1/r$ potential is no longer adequate. The correction to the electronic wave function due to the modified nuclear potential is known as the Breit-Crawford-Rosenthal-Schawlow correction.

Calculations of ϵ_{BCRS} take into consideration how the charge is distributed over the nucleus. Rosenthal and Breit considered for their calculation the charge

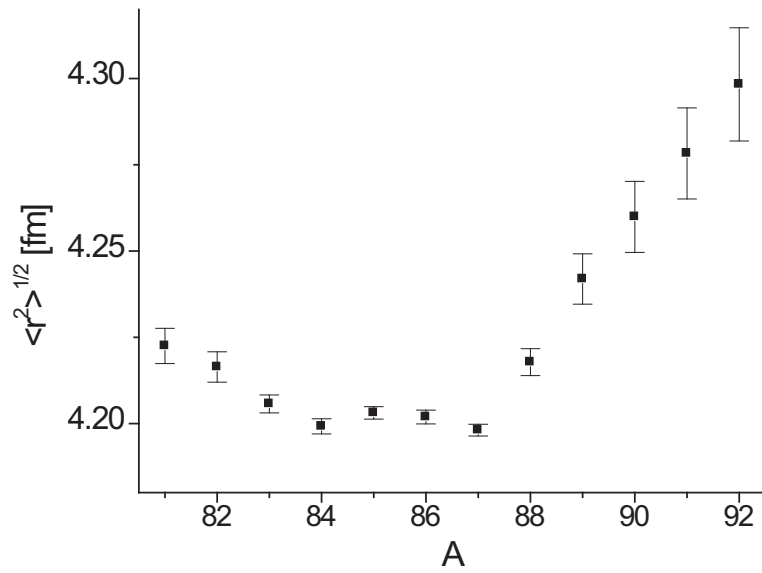


Figure 2.1: Plot of nuclear charge radius of rubidium as a function of atomic number. Adapted from Ref. [45].

	r_N [fm]	Ref.	ϵ_{BCRS}
^{85}Rb	4.2031(18)	[45]	0.0090835(34)
^{87}Rb	4.1981(17)	[45]	0.0090735(36)

Table 2.1: Values of ϵ_{BCRS} and corresponding nuclear radius for both rubidium isotopes.

to be on the surface of the nucleus [39]. Schawlow and Crawford also calculated the change of the wave function except they considered the charge to be uniformly distributed in the nucleus [40]. Rosenberg and Stroke proposed later a third model to improve the agreement between theory and experiment: a diffuse nuclear charge distribution [41].

The neutron and proton shells in rubidium determine the deformation as well as the spatial distribution of the nuclear charge. The neutron shell for ^{87}Rb is closed at magic number $N = 50$ making it impervious to the addition and subtraction of nuclear matter [45, 46]. The subtraction of two neutrons to form ^{85}Rb does not affect significantly the electric charge distribution, and the electric potential, compared to the one from ^{87}Rb , remains the same (see Fig. 2.1).

The expression of ϵ_{BCRS} for the uniformly charged sphere and charge on surface models is [47]:

$$\epsilon_{BCRS} = \frac{2(\kappa + \rho)\rho(2\rho + 1)}{(2\kappa + 1)(\Gamma(2\rho + 1))^2} \left(\frac{pZr_N}{a_0}\right)^{2\rho-1}, \quad (2.7)$$

where p is a constant of order unity, $\rho = \sqrt{\kappa^2 - (Z\alpha)^2}$, a_0 and α are the Bohr radius and fine structure constant, respectively, r_N is the nuclear radius, and κ is related

to the electronic angular momentum through the equation $\kappa = 1 + J(J + 1) - L(L + 1) - S(S + 1)$. Table 2.1 shows the value of the correction for a uniformly distributed charge as well as the nuclear radius of each isotope employed in the calculation.

Rosenfeld and Stroke propose a trapezoidal charge distribution to approximate their model. The interested reader should consult Ref. [41] for further explanation. All three models give relatively large ϵ_{BCRS} ($\sim 1\%$), however, the difference between both isotopes for all models is very small: $\epsilon_{BCRS}^{87} - \epsilon_{BCRS}^{85} \sim 10^{-5}$.

2.2.5 Bohr-Weisskopf effect

The interplay between nuclear magnetization with the magnetic field created by the atomic electrons causes the hyperfine splitting in atoms. A natural extension of hyperfine splitting measurements is to compare models of nuclear magnetism.

Nuclear magnetization is described in terms of nuclear moments with the biggest contribution coming from the nuclear magnetic dipole moment. The assumption of a point magnetic dipole gives good agreement between calculations and experiment, however it does not provide the complete picture. Nuclear magnetization has a finite volume. The electron wavefunctions of levels with total angular momentum $J = 1/2$ have a bigger overlap with the nucleus and are able to experience the subtle changes of the spatial distribution of the nuclear magnetization. These wave functions need to be modified to correctly account for the hyperfine splitting.

The corrections ϵ_{BW} to the wave functions due to a finite magnetization distri-

bution were first computed by Bohr and Weisskopf [42]. They assumed a uniformly distributed magnetization over the nucleus for their calculation with a predicted $\epsilon_{BW}^{87} - \epsilon_{BW}^{85}$ that ranges between 0.11% and 0.29%. The BW correction roughly scales as [42]:

$$\epsilon_{BW} \sim \left(\frac{Zr_N}{a_0}\right)\left(\frac{a_0}{2Zr_N}\right)^{2(1-\sqrt{1-(Z\alpha)^2})}\left(\frac{r^2}{r_N^2}\right)_{Av}, \quad (2.8)$$

where the average is taken over the magnetization distribution, with $(r^2/r_N^2)_{Av} = 3/5$ for a uniform magnetization. For rubidium this gives a correction of the order of 0.2%, however it is strongly dependent on spin and orbital states of the nucleons *i.e.* on the specifics of the nuclear magnetization. Stroke *et. al.* performed the same calculation using a trapezoidal magnetization distribution [48]. Their results agree very well with experimental information extracted from the ground state; they calculate a hyperfine anomaly difference of 0.33%. Both of these theoretical results are independent for the main quantum number of the valence electron [33], just as required by Bohr and Weisskopf.

The nuclear shell model predicts that the total magnetic dipole moment has contributions from both the proton and the neutron shell, each with orbital and spin angular momenta [33]

$$\vec{\mu} = \sum_{i=n,p} (g_{s,i}^{eff} \vec{s}_i + g_{l,i}^{eff} \vec{l}_i) \mu_N, \quad (2.9)$$

where g_s^{eff} and g_l^{eff} are the effective nuclear spin and nuclear orbital gyromagnetic ratios, respectively, \vec{s} and \vec{l} are the nuclear spin and nuclear orbital angular momenta

	Theory [μ_N]	Experiment [μ_N]	Ref.
^{85}Rb	2.00	1.35298(10)	[50]
^{87}Rb	2.64	2.75131(12)	[50]

Table 2.2: Theoretical and experimental values of the nuclear dipole moment for rubidium.

and the sum is taken over both shells. The g -factors have the values $g_s^{eff}=3.1(2)$ and $g_l^{eff}=1.09(2)$ [49].

The magnetic dipole moment in rubidium comes almost entirely from the vector addition of the orbital and spin angular momenta of a single valence proton. The neutron shell is almost spherical for both isotopes due to its closed shell structure and the contribution to the angular momentum from the neutron shell is very small.

The lighter of the two isotopes, ^{85}Rb , has the valence proton in an almost degenerate f orbital with its spin and orbital momenta antialigned yielding a value of $I=5/2$. Adding two more neutrons to the core shifts the energy level of the valence proton to the nearby p orbital and aligns both momenta giving the known value of $I=3/2$. Table 2.2 presents the theoretical prediction of the nuclear magnetic moment using Eq. 2.9 as well as the experimental result. It is indeed remarkable that such a simple model reproduces closely the experimental results, particularly for the closed nuclear shell structure of ^{87}Rb .

Three main factors make the two stable isotopes of rubidium good candidates for observing the BW effect. First the different orientation of the nuclear spin of the valence proton with respect to the nuclear orbital angular momentum. Second, the

small relative difference in nuclear charge deformation. Third, the change of orbital for the valence proton in the two isotopes.

2.2.6 Two-photon spectroscopy

We use atomic laser spectroscopy to measure the hyperfine splitting in two isotopes of rubidium. To reach the $6S_{1/2}$ state from the $5S_{1/2}$ ground state we need a two photon transition. We increase the probability of transition by using the $5P_{1/2}$ level as an intermediate step. We develop a theoretical model of the two-photon transition that includes the main physical aspects of our atomic system (see Fig. 2.2) based on a density matrix formalism.

Our experimental setup consists of two counter propagating laser beams going through a glass cell with rubidium vapor in a small magnetic field. We lock the laser at 795 nm on resonance, the middle step to the $5P_{1/2}$ level, while we scan the 1.324 μm laser (from here on referred to as the 1.3 μm laser) over the $6S_{1/2}$ level and observe the absorption of the 795 nm laser. The system can be modeled as a three level atom in which the on-resonance middle step enhances the excitation to the final step and the counter propagating laser beams help suppress the Doppler background (see for example Ref. [51]). However, numerical simulations show that we have to model our system as a five level atom to include its main qualitative feature: optical pumping effects increase the absorption of the 795 nm laser when the 1.3 μm laser is on resonance.

Figure 2.3 shows our simplified atomic model. We have neglected the Doppler

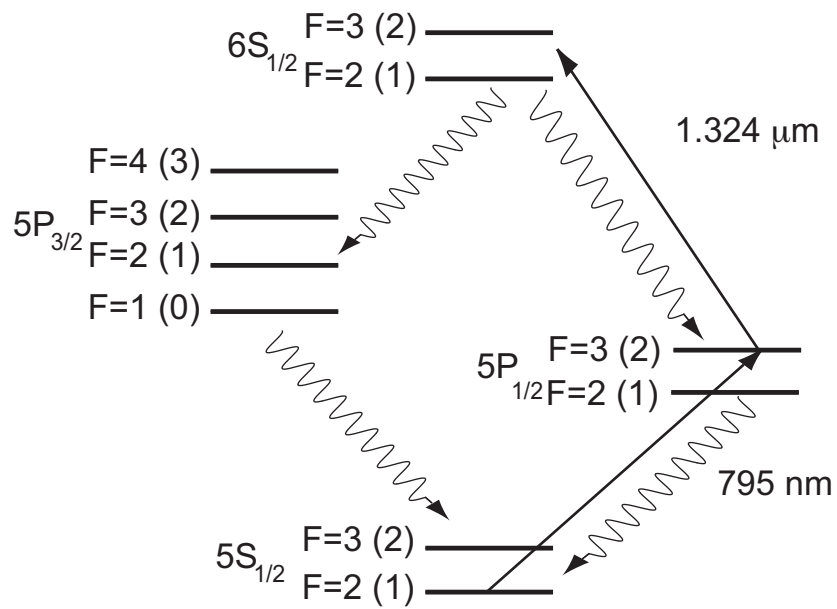


Figure 2.2: Energy levels relevant to our experiment (energy separations not drawn to scale). The numbers correspond to ⁸⁵Rb (⁸⁷Rb). Straight arrows correspond to the excitation lasers, undulated arrows to decays.

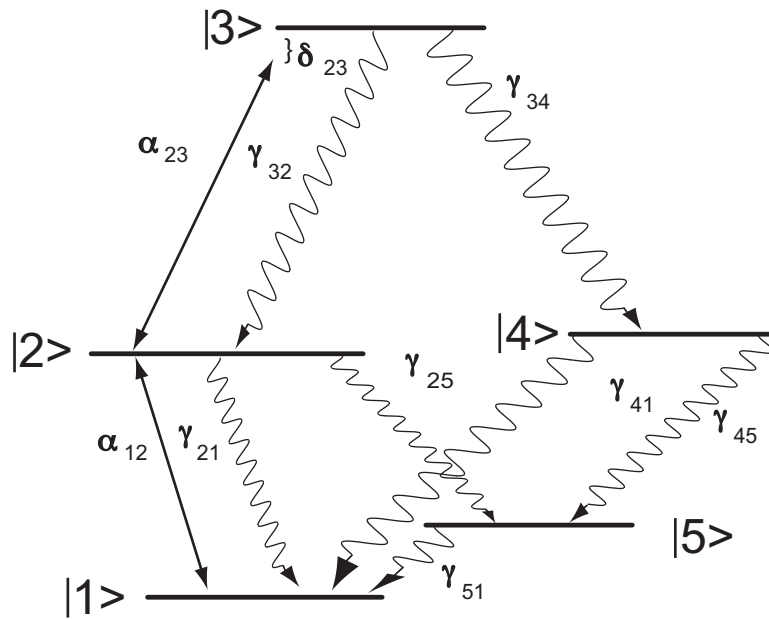


Figure 2.3: Energy level diagram of the theoretical model representing our system. The $\gamma_{i,j}$ correspond to the decay rate between levels $|i\rangle$, $|j\rangle$, $\alpha_{i,j}$ is the Rabi frequency relating levels $|i\rangle$ and $|j\rangle$, and δ_{23} is the detuning from resonance of the excitation laser between levels $|2\rangle$ and $|3\rangle$.

effects as well as the Zeeman sublevels in order to keep the calculation as simple as possible without losing the main qualitatively features of our system. Level $|1\rangle$ represents the lower hyperfine state of the $5S_{1/2}$ level while $|2\rangle$ is the upper hyperfine state of the $5P_{1/2}$. The decay rate between the two levels is $\gamma_{21}/2\pi = 6$ MHz [52]. We simplify the hyperfine states of the $6S_{1/2}$ level to just one level with decay rate $\gamma_{32}/2\pi = 3.5$ MHz [53]. The ground and intermediate levels are coupled by the Rabi frequency α_{12} while the intermediate and the excited levels are coupled by α_{23} . The remaining two levels, $|4\rangle$ and $|5\rangle$, represent all other decay channels out of the cascade system and the upper hyperfine ground level, respectively. The detuning between levels $|1\rangle$ and $|2\rangle$ is zero for our experiment, but we let the detuning between levels $|2\rangle$ and $|3\rangle$ vary as δ_{23} . The total population is normalized to one.

We are left with a set of twenty five linear equations for the slowly varying elements of the density matrix σ_{nm} after using the rotating wave approximation. These are

$$\sum_k (\gamma_{kn}\sigma_{kk} - \gamma_{nk}\sigma_{nn}) + \quad (2.10)$$

$$\frac{i}{2} \sum_k (\alpha_{nk}\sigma_{kn} - \sigma_{nk}\alpha_{kn}) = 0 \text{ for } n = m,$$

$$[i(\Omega_{nm} - \omega_{nm}) - \Gamma_{nm}]\sigma_{nm} + \quad (2.11)$$

$$\frac{i}{2} \sum_k (\alpha_{nk}\sigma_{km} - \sigma_{nk}\alpha_{km}) = 0 \text{ for } n \neq m,$$

where $\omega_{nm} = (E_n - E_m)/\hbar$ is the transition frequency, $\Omega_{nm} = -\Omega_{mn}$ is the laser frequency connecting the levels. The damping rate is given by:

$$\Gamma_{nm} = \frac{1}{2} \sum_k (\gamma_{nk} + \gamma_{mk}). \quad (2.12)$$

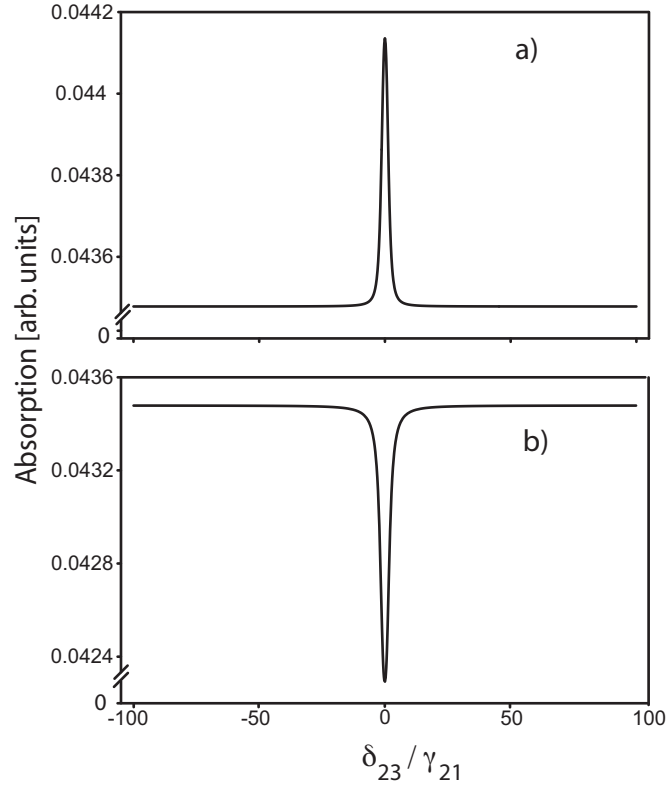


Figure 2.4: Numerical simulation of the absorption of the 795 nm laser as a function of the normalized detuning of the 1.3 μm laser to level $|3\rangle$ in units of γ_{21} . Both plots have the same parameters except for the ratio γ_{41}/γ_{45} . (a) Increase of absorption with $\gamma_{41}/\gamma_{45} = 2$. (b) Decrease of absorption with $\gamma_{41}/\gamma_{45} = 1/2$.

We solve for σ_{12} leaving the detuning between levels $|2\rangle$ and $|3\rangle$ ($\delta_{23} = \Omega_{23} - \omega_{23}$) as a free parameter. We plot the negative of the imaginary part of σ_{12} , which is proportional to the absorption of level $|2\rangle$, as a function of δ_{23} for several different sets of parameters. Our five level model reproduces the increase of absorption observed as the second excitation goes into resonance. This can be explained in the following way. The laser coupling levels $|1\rangle$ and $|2\rangle$, in the absence of the second excitation, pumps the atoms to level $|5\rangle$. In the steady state there will be little absorption due to a very small number of atoms being transferred from $|5\rangle$ to $|1\rangle$. By adding the second excitation a new reservoir of “fresh” unexcited atoms appears in level $|1\rangle$. Instead of falling to the non-absorbing level $|5\rangle$, they travel to level $|3\rangle$ and then decay to the initial ground state level through level $|4\rangle$. These “fresh” atoms will add to the ground state population and increase the absorption (see the Appendix).

Figure 2.4 shows samples of our simulation. We have plotted the absorption of the laser connecting levels $|1\rangle$ and $|2\rangle$ as a function of the detuning of the second laser. Figure 2.4 (a) shows how the absorption increases as the second laser goes on resonance while Fig. 2.4 (b) shows a decrease. Both plots have the same model parameters except for the ratio γ_{41}/γ_{45} . This ratio determines whether the atom will be lost or return to the cycle. A ratio bigger than one pumps atoms preferentially to level $|1\rangle$ rather than level $|5\rangle$ which constitutes a fresh reservoir of excitable atoms.

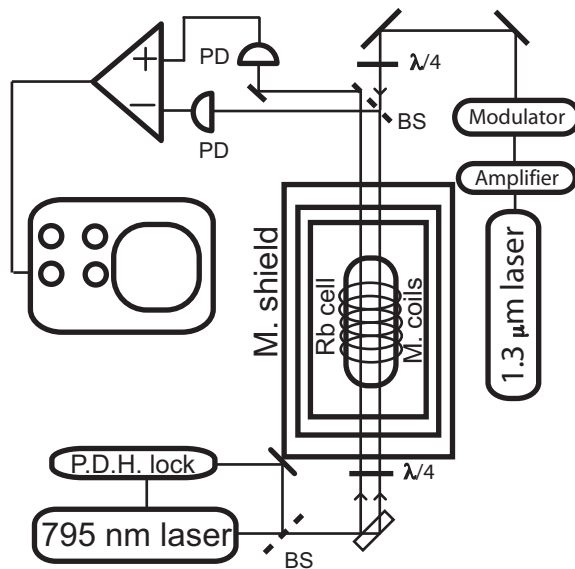


Figure 2.5: Block diagram of the experiment. Key for figure PD: photodiode, P.D.H.: Pound-Drever-Hall, M: magnetic, BS: beamsplitter.

2.3 Measurement of the hyperfine splitting

2.3.1 Apparatus

We use a Coherent 899-01 Titanium Sapphire (Ti:sapph) laser with a linewidth of better than 500 kHz tuned to the D1 line at 795 nm for the first step of the transition. A Pound-Drever-Hall (PDH) lock to the $F = 1(2) \rightarrow F = 2(3)$ transition in ^{87}Rb (^{85}Rb) in a separate glass cell at room temperature stabilizes the linewidth and keeps the 795 nm laser on resonance. An HP 8640B signal generator acts as the local oscillator for the lock. The 795 nm laser remains on resonance for about 40 minutes, much longer than the time it takes to record a single experimental trace.

A grating narrowed diode laser at 1.3 μm with a linewidth better than 500 kHz excites the second transition. We scan the frequency of the 1.3 μm laser with a triangular shaped voltage ramp from a synthesized function generator at 4 Hz applied to the piezo control of the grating and monitor its frequency with a wavemeter with a precision of $\pm 0.001 \text{ cm}^{-1}$. A fiber-coupled semiconductor amplifier increases the power of the 1.3 μm laser before it goes to a large bandwidth ($\approx 10 \text{ GHz}$) Electro-Optic Modulator (EOM). Another HP 8640B modulates this EOM. Fig. 2.5 shows a block diagram of the experimental setup.

A thick glass plate splits the 795 nm laser beam into two copropagating beams before going to the glass cell. The glass cell is 30 cm long and has a diameter of 2.5 cm. The rubidium glass cell was made at NIST using high vacuum and a 99.9% pure rubidium ampoule to minimize contaminants and with no buffer gas. The power of each beam is approximately 10 μW with a diameter of 1 mm. We

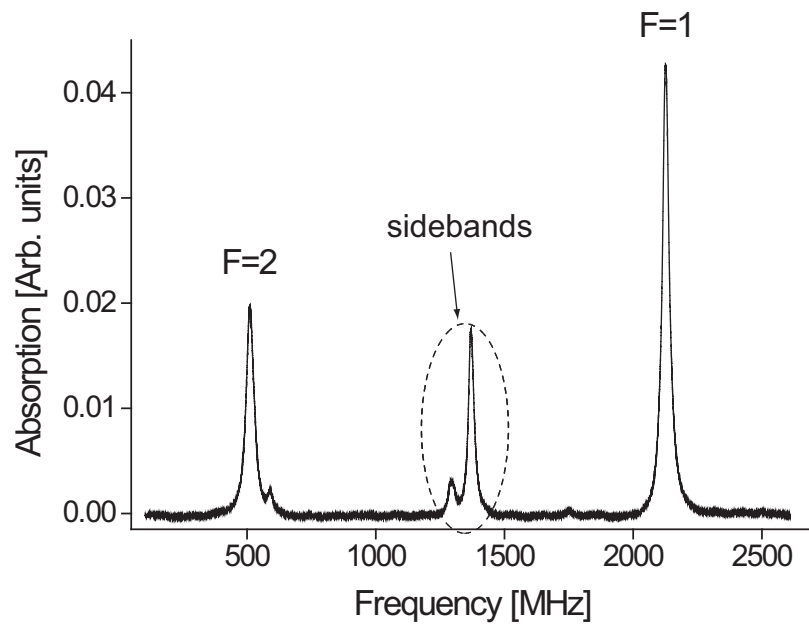


Figure 2.6: Absorption profile of the $6S_{1/2}$, $F = 1$ and $F = 2$ hyperfine states of ^{87}Rb with sidebands. The big sideband belongs to the $F = 1$ peak. The small feature on the side of the $F = 2$ peak corresponds to the second sideband of the $F = 1$ peak. The glass cell is in a magnetic field of 0.37 G.

operate in the low intensity regime to avoid power broadening, differential AC stark shifts and line splitting effects such as the Autler-Townes splitting. Both beams are circularly polarized by a $\lambda/4$ waveplate. A counter propagating $1.3 \mu\text{m}$ laser beam with a power of 4 mW and approximately equal diameter overlaps one of the 795 nm beams. The lasers overlap to a precision of better than 1 mm along 75 cm giving at most a diverging angle of 1 mrad.

The cell resides in the center of a 500-turn solenoid that provides a magnetic field of 7.4 Gauss/A contained inside a three layered magnetic shield to minimize magnetic field fluctuations [54]. The middle layer has a higher magnetic permeability to avoid saturation effects. The dimensions of the solenoid (70 cm long and a diameter of 11.5 cm) guarantees the uniformity of the magnetic field observed by the atoms. We operate under a weak magnetic field ($B \approx 1$ Gauss) to work in the Zeeman linear regime.

After the glass cell an independent photodiode detects each 795 nm beam. The outputs of the detectors go to a home-made differential amplifier to reduce common mode noise. A digital oscilloscope records the output signal for different values of modulation, polarization and magnetic field and averages for about three minutes. The order in which the absorption profiles are recorded is random. During the experimental runs we monitor the current going to the solenoid that provides the quantization axis. A thermocouple measures the changes in temperature inside the magnetic shield (24°C) to within one degree. The optical attenuation for the D1 line at line center is 0.4 for ^{85}Rb and about three times less for ^{87}Rb .

2.3.2 Method

We modulate the 1.3 μm laser to add sidebands at an appropriate frequency with a modulation depth (ratio of sideband amplitude to carrier amplitude) that ranges between 1 and 0.1. The sidebands appear in the absorption profile at a distance equal to the modulation from the main features and work as an *in situ* scale (see Fig. 2.6). We measure their separation as a function of the modulation for values bigger and smaller than half the hyperfine splitting. We interpolate to zero separation to obtain half the hyperfine splitting (see Fig. 2.7). This technique transfers an optical frequency measurement to a much easier frequency measurement in the RF range.

The size of the main peaks depends on the coupling strength between transitions; the size of the sidebands (as compared to the main peaks) will be determined by the strength of the transition and also on the number of sidebands simultaneously on or close to resonance. We observe under normal experimental conditions that the laser sidebands are both close to resonance (the lower frequency sideband to the $6S_{1/2} F = 1$ and the upper one to the $F=2$ transition) when the carrier is around the half point of the splitting. The stronger of the transitions ($F = 1$) depopulates the $5P_{1/2}, F = 2$ level leaving only a few atoms to excite with the upper sideband, hence the smaller transmission peak for the sideband corresponding to $F = 2$.

We have also observed a much richer atomic behavior by changing the laser intensities, polarizations and magnetic field environment of the glass cell. Optical pumping moves the atomic population from one level to another quite efficiently.

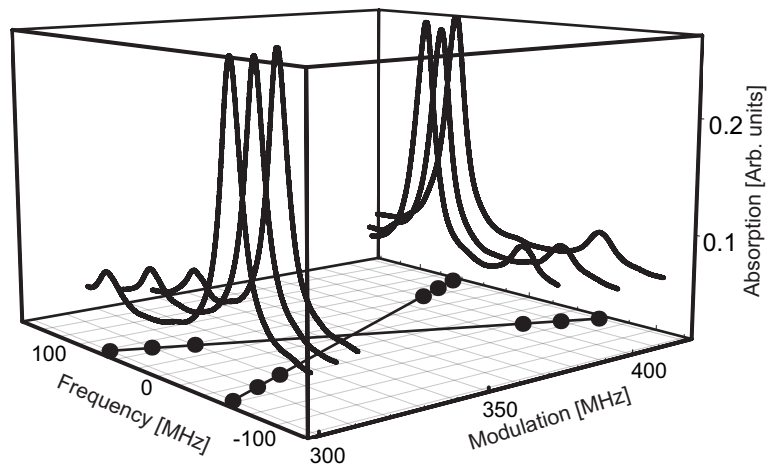


Figure 2.7: Experimental traces that illustrate sideband crossing for ^{85}Rb . The larger resonance corresponds to the $F = 2$ level, the smaller one to the $F = 3$ level of the $6S_{1/2}$ state. The dots correspond to the center of the profiles, the point where both lines cross corresponds to half the hyperfine separation.

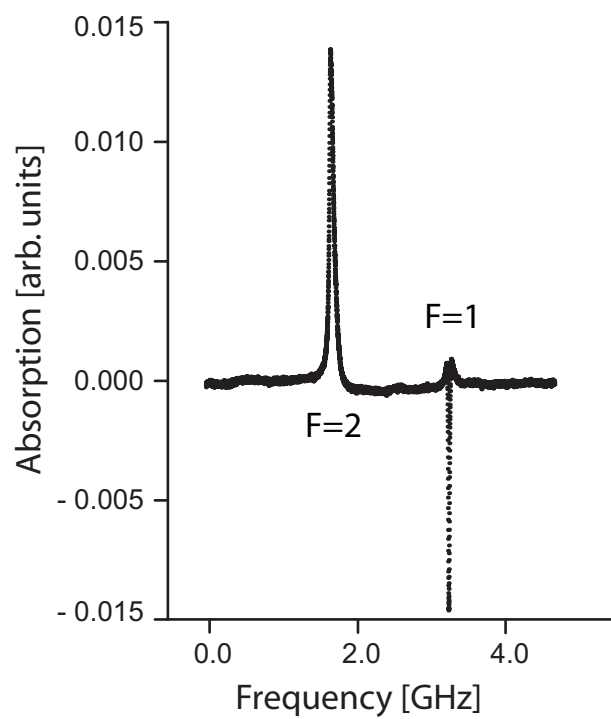


Figure 2.8: Experimental trace of absorption of the 795 nm laser for ^{87}Rb showing both increase and decrease of absorption due to optical pumping.

This is manifest in how the peaks change in magnitude or just switch from an increase of absorption to a decrease (see Fig. 2.8) just as our very simple theoretical model predicts. These effects point out that a careful control of the environment is necessary for a successful realization of the experiment.

The transfer of population by specific selection of polarization and magnetic environment can also be used to obtain a better experimental signal. There are several options to reach the $6S_{1/2}$ level. From the ground hyperfine states we can do $\Delta F = 0, \pm 1$ transitions. We find that doing the two step excitation in either a $\sigma^+ : \sigma^-$ or $\sigma^- : \sigma^+$ polarization sequence for the 795 nm and 1.3 μm lasers, respectively, with a $\Delta F = 1$ for the first step increases the amplitude of the signal. By choosing this polarization sequence we increase the probability of the atom going to the excited state and avoid placing it in a non-absorbing state [55].

We place the rubidium cell in a uniform magnetic field collinear with the propagation vectors of both lasers. The magnetic field provides a quantization axis as well as a tool to probe systematic effects. The hyperfine separation is now dependent on the magnetic field strength and the alignment with the laser. We measure the hyperfine splitting for different values of the magnetic field and polarization making sure that the above polarization sequence is always satisfied. We extract the value of the splitting at zero magnetic field from a plot of hyperfine splitting as a function of magnetic field.

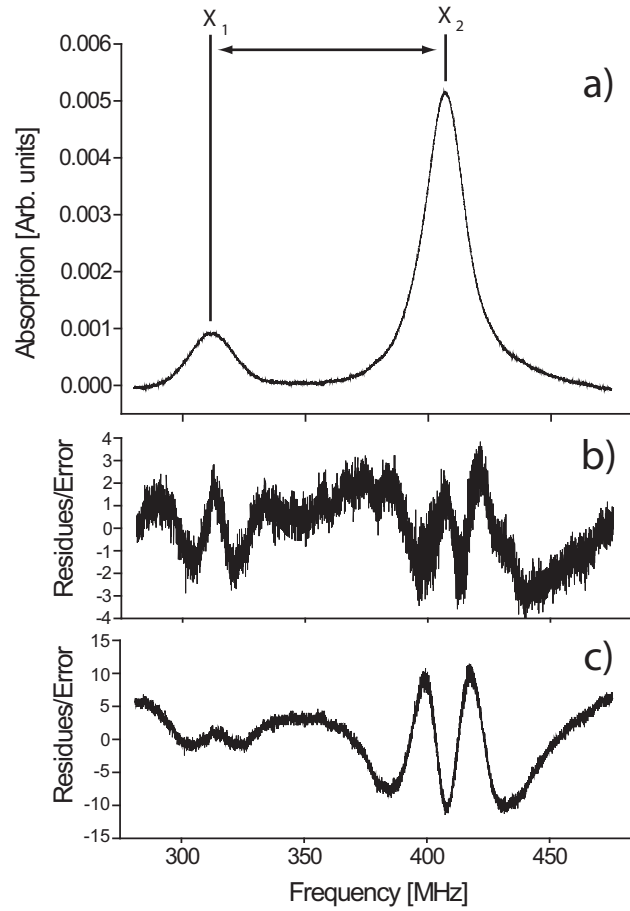


Figure 2.9: (a) Scan of the sidebands of the $6S_{1/2}, F=1$ and $F = 2$ hyperfine states of ^{87}Rb . The fits are not shown for clarity. (b) Normalized residuals of the Lorentzian fit, the reduced χ^2 is 2.13. (c) Normalized residuals of the Gaussian fit, the reduced χ^2 is 23.13.

2.3.3 Results and systematic effects

We study the contributions of several systematic effects that can influence the hyperfine separation measurement. We analyze the peak shape model for the non-linear fit to obtain the separation of the centers of the profiles, scan width and scan rate of the 1.3 μm laser, power of the 795 nm and 1.3 μm lasers, optical pumping effects, magnetic field effects, and temperature.

A) *Peak shape model and non-linear fit.* The absorption of a Doppler-broadened two level system as a function of laser detuning is a Voigt profile. When a multi-level system is considered it is not trivial to write down the functional form of the absorption of any of the lasers interacting with the system (see for example Refs. [56, 57]). We fit the experimental data to Voigt, Lorentzian and Gaussian functions to find the line centers and compare the results for consistency.

We use the non-linear fit package of ORIGINTM to fit the above mentioned profiles to search for model-dependent systematics. ORIGINTM uses a Levenberg-Marquardt algorithm to minimize the residuals given a specified error. The program has been used in the past by our group to obtain high precision lifetime measurements [14, 53]. We use the resolution limit of the 8 bit analog to digital converter of the scope for these calculations which corresponds to 0.5% of the total scale used. Lorentzian and Gaussian fits have three variable parameters to fit for each peak which correspond to the FWHM, the line center, the area under the curve plus a single offset for both peaks. Voigt profiles have an extra parameter which corresponds to the temperature of the sample. ORIGINTM gives the error of each

parameter which depends on the quality of the data.

Voigt profiles are in very good agreement with the lineshape. The fit yields the low temperature limit of the Voigt profile *i.e.* a Lorentzian, and hence is in agreement with the line center extracted using a Lorentzian profile. This is expected since the contribution of the Doppler effect to the resonance lineshape should be minimized by the counter propagating laser setup and by an expected group velocity selection arising from the two-step excitation process *i.e.* “two-color hole burning” (see Appendix A). The 795 nm laser will only interact with a small number of group velocities; these groups will be the only ones that will be excited to the $6S_{1/2}$ level by the 1.3 μm laser. Line centers extracted from Gaussian fits agree with results from the above mentioned profiles but decay too fast for frequencies far away from the centers. We also fit the data to a convolution of Lorentzian profiles with a rectangular transmission function and an exponential of a Lorentzian to search for systematic errors and to understand better our residues.

All peak shape models give consistent line centers consistent among themselves. All of them have similar structures in the residues within the line width of the resonances (see Fig. 2.9). We have determined that these features come about from the high sensitivity from deviations from a perfect fit that a difference of two peak profiles has. In other words, by taking the residues we are effectively taking the derivative of a peak profile that will be as sensitive as sharp the linewidth is. To further verify this we take the numerical derivative of the data to search for residual structure that might change our measurement (see Fig. 2.10). We fit a straight line to the data that lies within the linewidth and extract when the line crosses zero.

The results are consistent with the fits. Close analysis of the derivative in this region reveals no structure.

Of the fitted functions Lorentzians yield the smallest χ^2 . The fitting error of the line centers for all our data for Lorentzian fits range between 15 kHz and 30 kHz. We quote the average of all the fitting errors of our data in Table 2.3. Fig. 2.9 shows the magnified sidebands as well as the residues for a Lorentzian and Gaussian fits. We extract the line centers with both models; the difference in separation for both models is in this case $|x_1 - x_2|_{Lorentzian} - |x_1 - x_2|_{Gaussian} = 0.35(68)$ MHz. The reduced χ^2 of the non-linear Lorentzian fit for all our data ranges between 1 and 10 depending on the noise of the signal with a χ^2 average of 2.4 over twenty fits. We do not observe changes in the splitting that depend on the frequency range fitted around the resonances.

The relative angle between both copropagating lasers induces a systematic shift on the absolute frequency the atoms observe due to the appearance of the $\vec{v} \cdot \vec{k}_i$ dependence on absorption where \vec{v} is the velocity of the atom and \vec{k}_i is the wave vector for either laser. This angle dependence on the Doppler shift for our system is almost the same for both our lasers since the cosine of the angle between them differs from one by one part in 10^5 . Furthermore, any residual effect is minimized since we measure frequency differences.

Just like the lines shape, analytic expressions for the linewidth are difficult to write down. We perform a numerical simulation of our five level system presented in Subsection 2.2.6 of the theoretical background in the presence of a room temperature velocity distribution. The resonances show linewidths of the order of 30-40 MHz

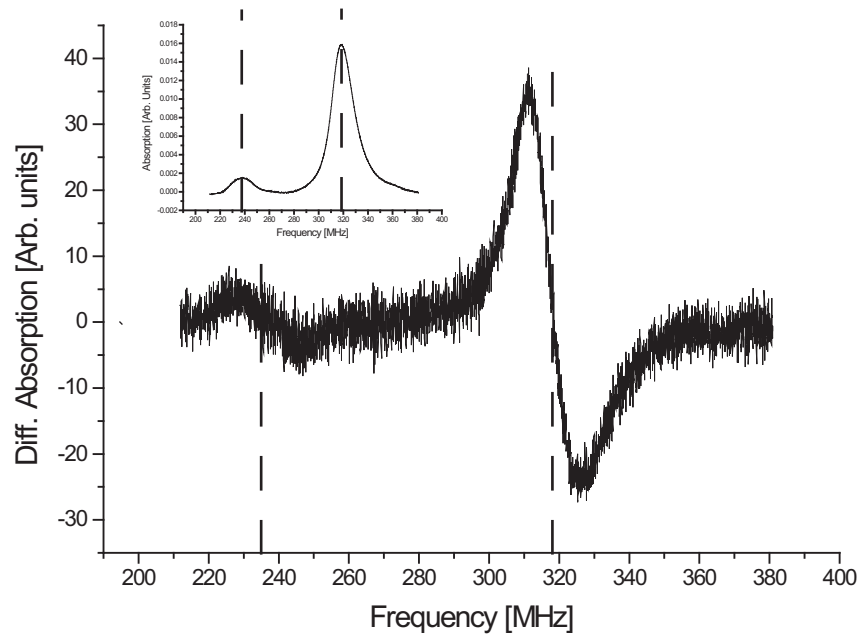


Figure 2.10: Numerical derivative of the sidebands of ^{85}Rb in a magnetic field of 1.8 G. The inset shows the original signal. The dotted lines mark the crossing through zero which corresponds to the line center in the original data.

which are in very good agreement with experimental results.

Distortions of the lineshape *i.e.* asymmetries, depend on the detuning of the 795 nm laser from resonance. These can induce unwanted systematic errors to the measurement. Numerical simulations show, following Ref. [11], that the separation of the hyperfine splitting depends negligibly on the detuning from the *D1* line. Nevertheless, we look for any asymmetries in the peaks themselves and dependence on the direction of scan during experimental runs. No correlation with these effects is found.

We interpolate to zero from a plot of distance between the center of the sidebands *vs.* the modulation frequency to obtain half the hyperfine separation. The linear regression coefficients in this plots differ from one at the most in 2 parts in 10^4 . Typical errors for the crossovers amount to about 200 kHz.

B)*Scan and linearity of 1.3 μm laser.* Non-linearities in the piezo driving the feedback grating, hysteresis effects as well as a slow thermal drift on the 1.3 μm laser can generate undesired systematics in the measurement. We look for non-linearities by sending the voltage monitor of the piezo to a digital scope with an 8-bit resolution during the experimental runs as well as monitor the absorption peaks for asymmetries. Comparison between absorption peaks for both types of scan (low to high frequency and vice versa) reveals no systematic effects. Analysis of the long term drift of the 1.3 μm laser shows a stability of better than 100 kHz over a 5 min. period which is longer than the time we need to take a single experimental absorption signal.

C)*Power of the 795 nm and 1.3 μm laser.* We look for systematic dependence

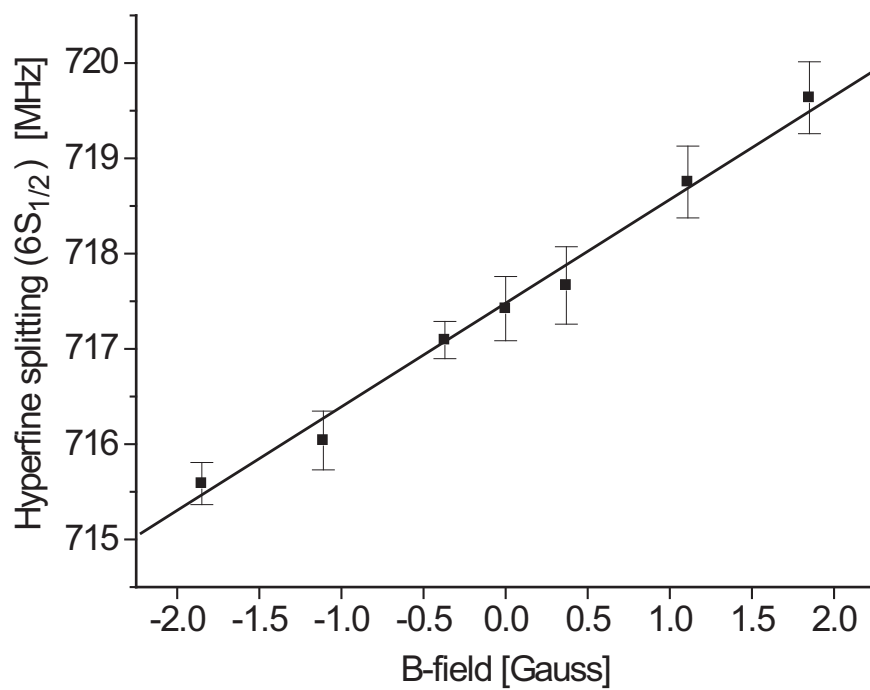


Figure 2.11: Zeeman plot of the hyperfine separation of the $6S_{1/2}$ level of ^{85}Rb with both lasers circularly polarized to better than 95% and linear fit.

on the hyperfine splitting on the power of both lasers. We change the power of the 795 nm laser from 4 μW to 40 μW while keeping the power of the 1.3 μm laser constant. Low signal to noise ratio and the observation of the Autler-Townes splitting determine the lower and upper boundaries of this interval, respectively.

The Autler-Townes effect predicts a splitting of the middle energy level by the on-resonance first step in a three level system that is proportional to the square root of its intensity [58]. For our typical experimental conditions the splitting should be less than 4 MHz, too small to be resolved with the observed linewidths of the atomic resonances (~ 40 MHz).

The 1.3 μm laser operates very close to its maximum power under normal experimental conditions. The power is distributed among the sidebands and the main carrier depending on the modulation depth. We gradually decrease the power of the 1.3 μm to half its operating value to detect any dependence on the power. We observe no correlation.

D) *Optical pumping effects and magnetic field.* Optical pumping effects are the most delicate of all the systematic effects. Both laser beams are carefully polarized using appropriate $\lambda/4$ waveplates and their polarization checked with a rotating polarizer in front of a detector to better than 95%. The polarization of the lasers as well as their alignment with the magnetic field determine the relative size of the peaks (m_F sublevels) that form the resonances of the $6S_{1/2}$ hyperfine levels. Comparison of absorption profiles for a set polarization sequence for different values of the magnetic field gives qualitative information of the alignment between the magnetic field and the lasers. The positive and negative magnetic field orientations in a

perfectly symmetric situation, after a switch of polarization sequence, should yield the same absorption profile. For everyday experimental conditions (around 1 G) we observe no difference between positive and negative magnetic field directions. We see broadening of the profiles at magnetic fields twenty times larger but no asymmetries. Differences start appearing at around 85 G which suggests good alignment between the lasers and the magnetic field as well as good control of the polarization of both lasers.

The hyperfine separation *vs.* magnetic field plot provides more quantitative information. Eq. (3) states that the plot should be linear with no discontinuities as we change the value of the magnetic field from positive to negative. Our plots show a smooth transition between negative and positive values of the magnetic field within experimental error. Fig. 2.11 shows a sample of our data when both lasers are circularly polarized to better than 95%.

We monitor the current of the coil generating the magnetic field to detect any fluctuation in the intensity of the field. We observe small fluctuations of the order of mG from current noise.

E) *Temperature.* We analyze the position of the absorption peaks as a function of temperature of the cell to check for related systematic effects such as collision shifts for both isotopes. The temperature of the glass cell is increased from room temperature (23°C) up to 40°C using a heat tape wrapped around it. While recording data we turn off the heating tape to avoid stray magnetic fields generated by the current going through it. The temperature of the glass cell is monitored with a thermocouple inside the magnetic shield with an accuracy of one degree. No dependence

Systematic effects	ν_{HF}^{85} [MHz]	ν_{HF}^{87} [MHz]
Optical pumping effects	≤ 0.016	≤ 0.029
Power of 795 nm laser	≤ 0.020	≤ 0.005
Power of 1.3 μm laser	≤ 0.011	≤ 0.011
Atomic density	≤ 0.020	≤ 0.010
Non linear fit	≤ 0.028	≤ 0.023
B-field fluctuations	≤ 0.015	≤ 0.025
Total Systematic	≤ 0.047	≤ 0.047
Statistical error	0.100	0.160
TOTAL	0.110	0.167

Table 2.3: Error budget for the hyperfine splitting measurement

on temperature is found.

We have concluded after close analysis of these studies that, to the accuracy of our measurement, Gaussianly distributed statistical fluctuations dominate our experiment (see Table 2.3). The statistical error in the hyperfine splitting, as stated by the standard error of the mean, is 110 kHz for ^{85}Rb and 167 kHz for ^{87}Rb .

Figure 2.12 shows the values of the magnetic dipole constant for ^{85}Rb for all experimental runs of this work. The final result for each run is determined by an interpolation to zero magnetic field as a function of the current in the solenoid.

Table 2.4 contains the measurements of the hyperfine splitting of the $6S_{1/2}$ level as well as the corresponding values of the magnetic dipole constants for both isotopes.

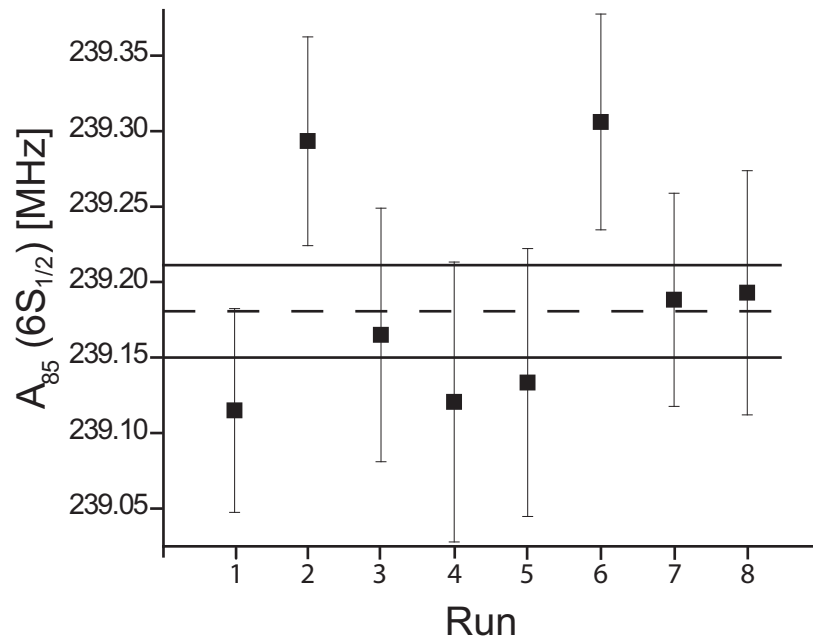


Figure 2.12: Results of different runs of the magnetic dipole constants of the $6S_{1/2}$ state of ^{85}Rb . The dashed line corresponds to the mean, the solid lines to the $1\text{-}\sigma$ error.

	^{85}Rb [MHz]	^{87}Rb [MHz]
ν_{HF}	717.54(10)	1615.32(16)
A	239.18(03)	807.66(08)

Table 2.4: Hyperfine splittings (ν_{HF}) and magnetic dipole constants for the $6S_{1/2}$ level.

The precision of our data allows us to observe a hyperfine anomaly. We use the values of Ref. [59] for the ratio $g_I^{85}/g_I^{87} = 0.295055(25)$. This is consistent with the experimental values of Ref. [50]. Using this value and our experimental results in Eq. 2.6 we obtain a value for the hyperfine anomaly difference of $_{87}\delta_{85} = -0.0036(2)$. This is less than a one percent difference, well beyond the current MBPT theoretical calculation accuracy of the hyperfine splittings.

2.4 Comparison with theory

We compare in Figs. 2.13 and 2.14 the results from this experiment with the previous experimental results of Gupta *et al.* [60] and the theoretical predictions of Ref. [34]. The hyperfine anomalies are still not within reach of *ab initio* MBPT so the value of ^{85}Rb comes from the value of ^{87}Rb considering no hyperfine anomaly.

2.5 Conclusions

We have measured the hyperfine splittings of the $6S_{1/2}$ level of ^{85}Rb and ^{87}Rb to a precision of 103 ppm and 153 ppm, respectively. Our measurement is consistent

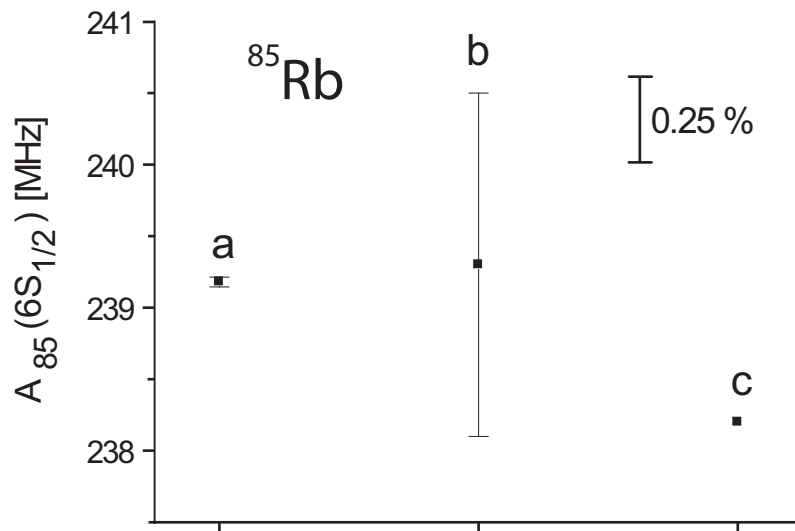


Figure 2.13: Comparison between experimental and theoretical results of the magnetic dipole constant of the $6S_{1/2}$ state of ^{85}Rb . The points labeled “a” and “b” correspond to our work and the work of Ref. [60], respectively. Point “c” corresponds to the theoretical prediction of Ref. [34].

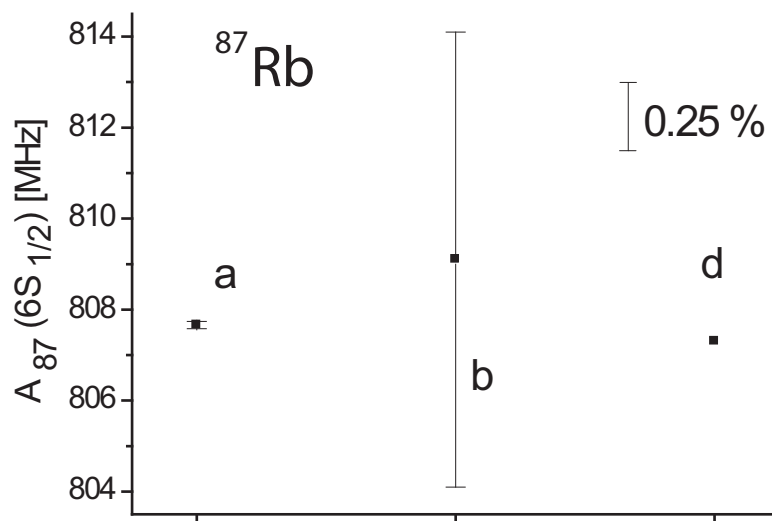


Figure 2.14: Comparison between experimental and theoretical results of the magnetic dipole constant of the $6S_{1/2}$ state of ^{87}Rb . The points labeled “a” and “b” correspond to our work and the work of Ref. [60], respectively. Point “d” corresponds to the theoretical prediction of Ref. [34] considering a non extant hyperfine anomaly.

	SDpT [MHz]	CCSD [MHz]	Experiment [MHz]
$5S_{1/2}$	1011.1	1020.086	1011.910813(2) [61]
$5P_{1/2}$	120.4	119.192	120.499 (10) [22]
$6S_{1/2}$	238.2		239.18(3) (this work)
$6P_{1/2}$	39.02		39.11(3) [25, 62]
$7S_{1/2}$	94.3		94.658(19) [27]

Table 2.5: SDpT and CCSD theoretical predictions calculated using *ab initio* MBPT from Ref. [34] and Ref. [35], respectively, and experimental magnetic dipole constants for the first $J=1/2$ levels in ^{85}Rb .

with and decreases the uncertainty of the past measurements [60] by a factor of 63 for ^{87}Rb and by a factor of 30 for ^{85}Rb [63].

Table 2.5 shows the values of the magnetic dipole constants using relativistic MBPT [34, 35] with single double partial triple (SDpT) wave functions, coupled-cluster single-double (CCSD) wave functions, and values extracted from measurements of the hyperfine splitting in other electronic states currently in the literature for $J=1/2$ [22, 25, 27, 61, 62]. We have not been able to find in the literature values for higher levels with adequate precision to include them in the figure. The agreement of the theory with the experiment, for $J=1/2$ levels, is well within the 1% level.

We are able to extract the hyperfine anomaly with our experimental data and show that precision measurements of the hyperfine structure in atomic states with different radial distributions can give information on the nuclear magnetization

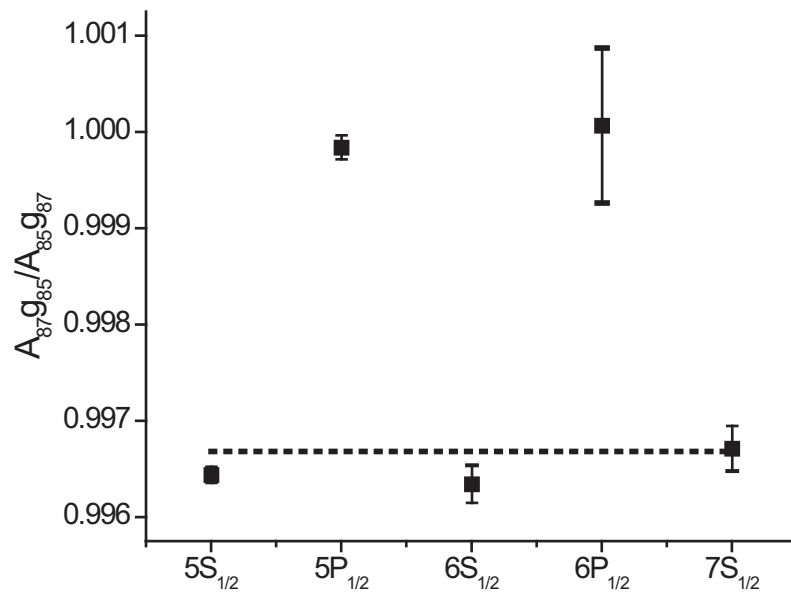


Figure 2.15: Hyperfine anomalies of other atomic levels of rubidium along with the value for the $6S_{1/2}$ level obtained in this measurement. The dashed line corresponds to the theoretical prediction for a diffuse magnetization distribution [48]. See text for references.

${}_{87}\delta_{85}$	
$5S_{1/2}$	-0.00356(8) [61]
$5P_{1/2}$	-0.0001(1) [22]
$6S_{1/2}$	-0.0036(2) (this work)
$6P_{1/2}$	0.0000(8) [25, 62]
$7S_{1/2}$	-0.0032(2) [27]

Table 2.6: Hyperfine anomaly differences ${}_{87}\delta_{85}$ for the first $J=1/2$ levels in rubidium.

distribution. The hyperfine anomaly difference we extract for the $6S_{1/2}$ is ${}_{87}\delta_{85} = -0.0036(2)$ [64]. The difference in the anomalies is indeed a factor of thirty larger than the expected BCRC contribution and it comes from the BW effect. Fig. 2.15 shows that the anomaly measured with the $nS_{1/2}$ levels is the same independent of the principal quantum number as well as the smaller deviation from the point interaction, if any, for the $nP_{1/2}$ levels [22, 25, 27, 61, 62, 63]. Table 2.6 shows the hyperfine anomaly differences for the first $J = 1/2$ levels.

The Bohr-Weisskopf effect predicts that the size of the effect is independent of the principal quantum number n . The plot and the table confirm this as well as the larger effect on the S states [42]. These new measurements invite new calculations of atomic properties and constrain nuclear calculations. As the nuclear charge and magnetization distribution are better understood they will further test and refine the calculations which are of crucial importance for PNC experiments.

Chapter 3

Measurements of lifetimes of excited states of francium and rubidium

3.1 Introduction

The lifetime of an excited state in an atomic system depends on the expectation value of the dipole operator $e\vec{r}$ between an initial and a final state wave functions [32]. In addition to being tools for tests of atomic structure, measurements of excited states lifetimes are the perfect complement for studies of hyperfine splittings since it is the behavior of the electronic wave function far away from the nucleus that becomes important. We present in this chapter the measurement of the lifetime of the $8s$ excited state in francium and the lifetime of the $5D_{3/2}$ state of rubidium. The measurement of the lifetime of the other state of the $5d$ manifold, the $5D_{5/2}$, can be found in our recent publication [65].

The $8s$ state is the preferred candidate for an optical PNC measurement: the dipole-forbidden excitation between the $7S_{1/2}$ ground state and the $8S_{1/2}$ state becomes allowed through the weak interaction. The equivalent transition in cesium has been used by the Boulder [5, 6] and Paris [66] groups and a quantitative understanding of the $8S_{1/2}$ state (its lifetime and its branching ratio) is critical to the successful extraction of weak-interaction physics in these experiments.

The work in rubidium presents the opportunity to measure the lifetime of the seldom studied d states. These states are becoming more important not only in

the study of fundamental symmetries [67, 68, 69], but also in quantum information science as they are used for qubit manipulation in ion traps [70, 71]. Safronova *et al.* [72] have shown the important role of high order corrections, up to third order, in calculations that use MBPT of the $5d$ states lifetimes. Previous experimental work on the lifetime of the $5D_{3/2}$ state [73] achieved a precision inferior to the atomic calculations. Our work improves the previous measurement by more than a factor of ten the precision which is essential for comparison with current and future atomic structure calculations.

The measurements we are presenting have been done in two different locations. The measurement of the $8S_{1/2}$ level was performed in the online dry film coated glass cell at Stony Brook [14] while the $5d$ manifold was measured at the University of Maryland [65].

This chapter starts with a brief introduction followed by the theoretical background (Section 3.2). Section 3.3 explains the experimental setup and the method used in each of the measurements. Section 3.4 presents the results and studies of probable systematics. Section 3.5 compares our results with theory and Section 3.6 has the conclusions.

3.2 Theoretical background

The lifetime τ of an excited state is related to partial lifetimes τ_j associated with each of the allowed decay channels. Each decay channel will be a function of the matrix element of the dipole operator between the initial state and the state

it decays to. The connection between the lifetime, partial lifetimes, and matrix elements are [72]

$$\frac{1}{\tau} = \sum_j \frac{1}{\tau_j} = \sum_j \frac{4}{3} \frac{\omega_{el_j}^3}{c^2} \alpha \frac{|\langle J_e || r || J_{l_j} \rangle|^2}{2J_e + 1}, \quad (3.1)$$

where ω_{el_j} is the transition energy, c is the speed of light, α is the fine-structure constant, J_e and J_{l_j} are, respectively, the initial and final state angular momenta, and $\langle J_e || r || J_{l_j} \rangle$ is the reduced matrix element. Eq 3.1 connects the lifetime of an excited state to the electronic wave functions of the atom. Because of the presence of the radial operator comparisons of measurements with theoretical predictions test the quality of the computed wave functions especially at large distances from the nucleus. Theorists need to calculate the transition energies and reduced matrix elements to predict lifetimes. MBPT has proven itself quite successful in predicting lifetimes. For a brief explanation of the method see Section 2.2.

3.3 Measurement of lifetimes of excited states

3.3.1 Time correlated single photon counting method

We adapt the time correlated single photon counting method [74] with a cold sample of atoms in a MOT to measure the lifetime of the excited states of francium and rubidium. The method consist of recording the time it takes to detect a single photon after the atomic sample has been excited by a one or two laser pulses that prepare the atoms in the state to be studied.

The single photon counting technique refers to the fact that we record at most one photon in one duty cycle. It is possible to record more than one photon in one

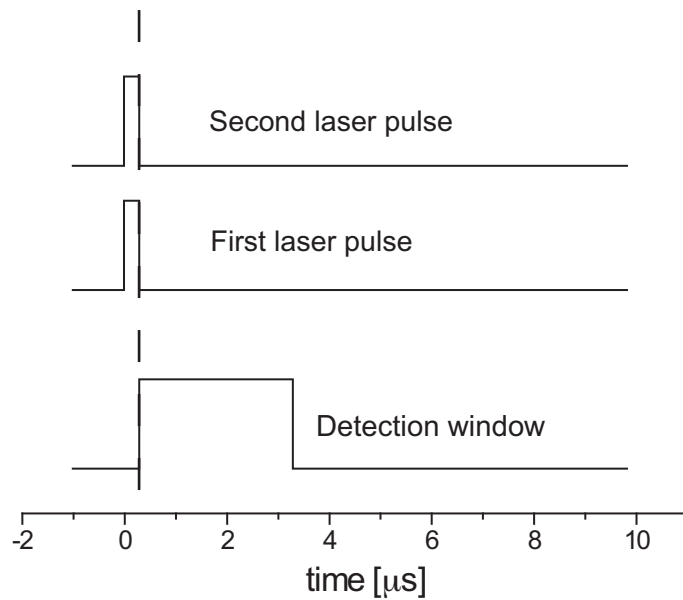


Figure 3.1: General scheme for time correlated single photon counting. The dotted line corresponds to the start of the decay of the fluorescence.

cycle, but once the electronics after the detector record one signal, it will not accept another one until a new cycle begins. This method works best when the probability of detecting more than one photon in one cycle is very small, which in turn keeps the corrections low. See Fig. 3.1 for a typical duty cycle.

3.3.2 Experimental setup

3.3.2.1 $8s$ state of francium

The production, cooling, and trapping of Fr online with the superconducting linear accelerator at the Nuclear Structure Laboratory has been described previously [8]. Briefly, a 100-MeV beam of five times ionized ^{18}O ions from the accelerator impinges on a gold target to make ^{210}Fr with radioactive half-life of about 3 min. We extract 10^6 francium ions/s from the interaction region and transport them to our laboratory where a cold yttrium foil neutralizes the atom. Francium resides on the foil long enough to rotate the neutralizer foil and close the trap and heat the foil for one second to release the atoms into the dry film coated glass cell where they are cooled and trapped (see Figs. 3.2 and 3.3). The cycle of accumulating and trapping repeats every 20 s.

Figure 3.4 shows the states of ^{210}Fr relevant for trapping and for the lifetime measurement. A Coherent 899-21 Ti:sapph laser operating at 718 nm excites the trapping and cooling transition $7S_{1/2}, F = 13/2 \rightarrow 7P_{3/2}, F = 15/2$. A Coherent 899-21 Ti:sapph laser operating at 817 nm repumps any atoms that leak out of the cooling cycle via the $7S_{1/2}, F = 11/2 \rightarrow 7P_{1/2}, F = 13/2$ transition (repumper in

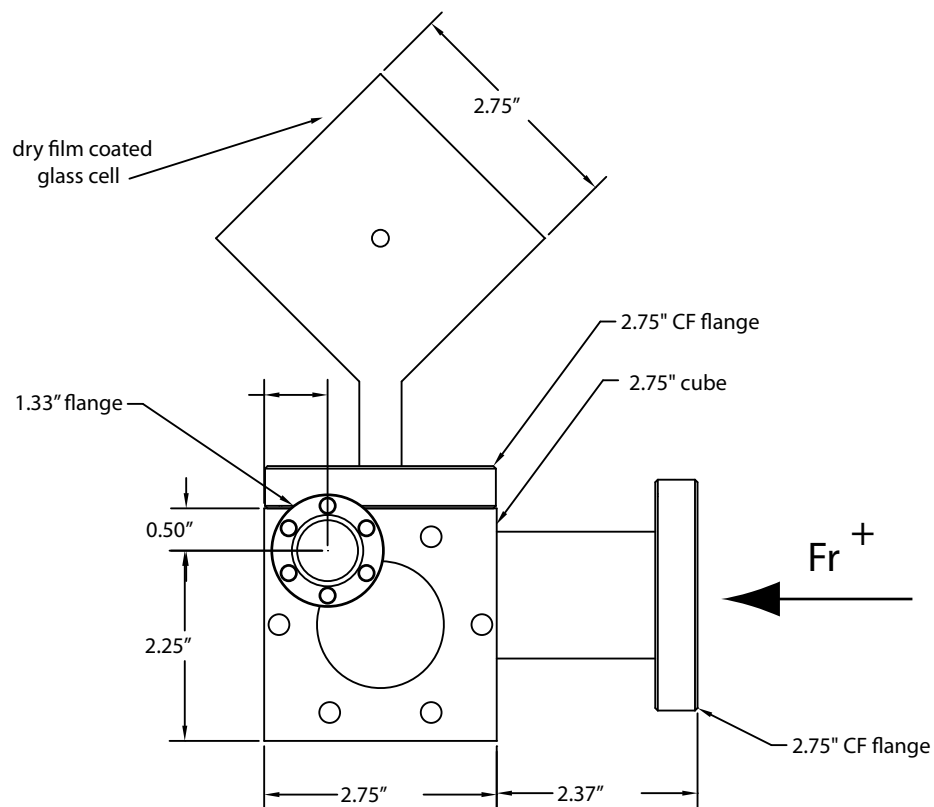


Figure 3.2: Dry film coated glass cell used to trap francium and neutralizer mechanism. The arrow points out the incoming direction of the francium ions.

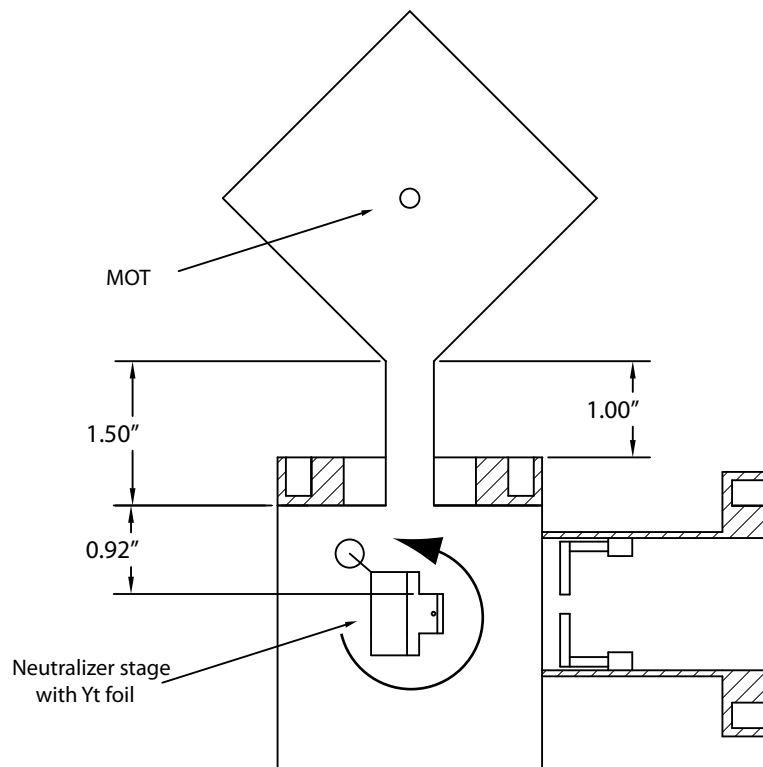


Figure 3.3: Cut out view, the arrow points out the direction of the rotation of the neutralizer stage.

Fig 3.4). We perform a two-step transition to reach the $8s$ level where the first step comes from a Coherent 899-01 Ti:sapph at 817 nm. The second step at $1.3 \mu\text{m}$ originates from an EOSI 2010 diode laser. A Burleigh WA-1500 wavemeter monitors the wavelength of all lasers to about $\pm 0.001 \text{ cm}^{-1}$. We lock the trap, first step, and repumper lasers with a transfer lock [75]. The $1.3 \mu\text{m}$ laser is frequency stabilized with the aid of a Michelson interferometer that is locked to the stabilized Helium-Neon laser from Melles Griot (model 05 STP 901) used in the transfer lock. The typical frequency drift of this laser is $\pm 0.8 \text{ MHz}$ in one hour and $\pm 1.2 \text{ MHz}$ in 8 hours *i.e.* a drift of $\approx 2 \text{ ppb}$ [75].

The MOT consists of three pairs of retroreflected beams, each with 15 mW/cm^2 intensity, 3 cm diameter ($1/e$ intensity), and red detuned 31 MHz from the atomic resonance. A pair of coils generates a magnetic field gradient of 9 G/cm. We work with traps of $< 10^4$ atoms, with a temperature lower than $300 \mu\text{K}$, with a diameter of 0.5 mm and a typical lifetime between 5 and 10 s. Both lasers of the two step excitation are on for 50 ns before they are switched off, while the counting electronics are sensitive for 500 ns to record the excitation and decay signal. The trap laser turns off 500 ns before the two-photon excitation. We repeat the cycle at rate of 100 kHz.

We modulate the trap light with an EOM from Gsänger (model LM0202) and an acousto-optic modulator (AOM) from Crystal Technologies (model 3200-144). The combination of the two gives an extinction ratio of better than 1600:1 after 500 ns. Other AOM's from Crystal Technology (model 3200) modulate the light of the repumper with an extinction ratio of 109:1 in a time of 30 ns after the pulse turns

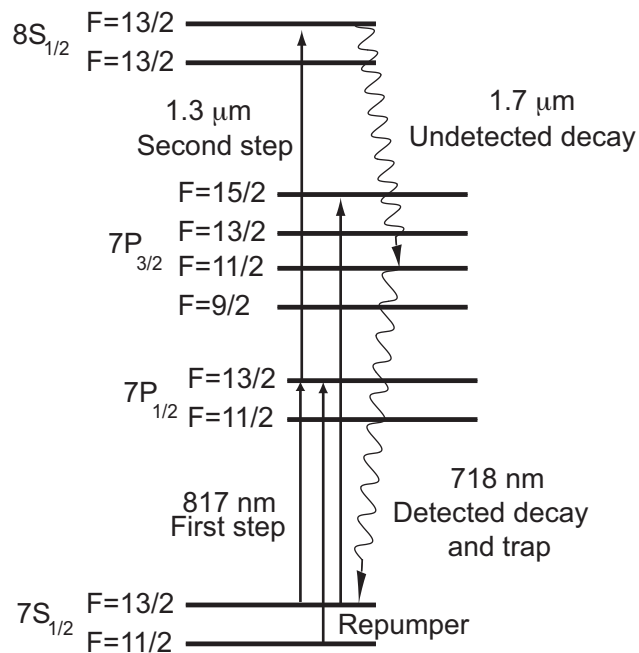


Figure 3.4: Energy levels used in the measurement of the $8s$ state of francium. The trapping and repumping lasers are also shown. The energy separations are not drawn to scale.

off.

We couple the $1.3\ \mu\text{m}$ laser into a single-mode optical fiber and pass it through a 10-Gbit/s lithium-niobate electro-optic fiber modulator from Lucent Technologies, then amplify it, and again modulate it with a second electro-optic fiber modulator from Lucent Technologies (model 2623N). The result is an on-off ratio of better than 1000:1 in a time of 20 ns.

We monitor the number of atoms in our trap using a 1:1 imaging system ($f/3.9$) and a CCD camera from Roper Scientific (model MicroMax 1300YHS-DIF). A 718 nm interference filter in front of the camera reduces background light. A 50/50 beam splitter in the imaging system sends half of the light to a photo-multiplier tube (PMT) from Hamamatsu (model R636).

After we turn off the excitation lasers, the atoms decay back to the ground level using two different decay paths (see Fig. 3.4). First, by emitting a $1.3\ \mu\text{m}$ photon it decays back to the $7P_{1/2}$ state and then fluoresces 817 nm light to return to the $7S_{1/2}$ ground state. The second possible decay channel is the $8S_{1/2} \rightarrow 7P_{3/2} \rightarrow 7S_{1/2}$ cascade decay. The $1.7\ \mu\text{m}$ fluorescence from the first step of this path is unobserved, but we detect 718 nm light from the second part of the decay. With the known lifetime of the $7P_{3/2}$ state, it is possible to extract the $8s$ level lifetime from the cascade fluorescence decay.

We amplify the photo-current pulses from the PMT with an Ortec amplifier (model AN106/N). We monitor a small time region with an EG&G gate (model LG101/N) and send the pulses to a constant fraction discriminator (CFD) from Ortec (model 934). The output of the CFD starts a gated time-to-amplitude converter

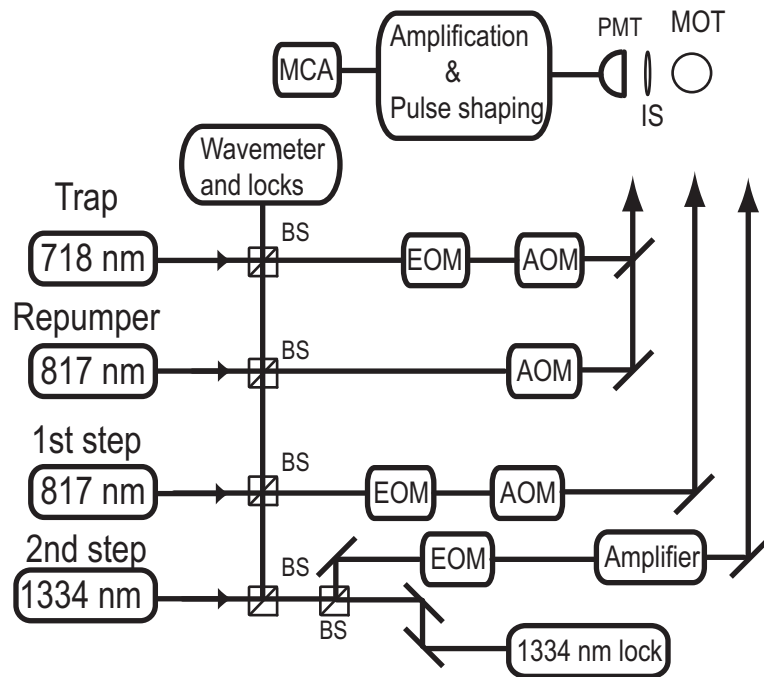


Figure 3.5: Block diagram of the experiment of the measurement of the lifetime of the $8S_{1/2}$ state of francium. Key for figure PMT: photomultiplier tube, AOM.: acousto-optical modulator, EOM: electro-optical modulator, IS: imaging system, MCA: multichannel analyzer. Timing electronics not shown.

(TAC) from Ortec (model 467) which we stop with a fixed-time-delay pulse after the two-photon excitation. We use a multichannel analyzer (MCA) from EG&G (model Trump-8k) to produce a histogram of the events showing directly the exponential decay. A pulse generator from Berkeley Nucleonics Corporation (model BNC 8010) provides the primary timing sequence for the measurement See Fig. 3.5.

3.3.2.2 $5D_{3/2}$ state of rubidium

We use our new science chamber to perform the measurement of the lifetimes of the $5d$ manifold. A rubidium dispenser works as the vapour source from which we load atoms into the MOT. The pressure inside the vacuum chamber is better than 10^{-10} torr. A pair of anti-Helmholtz coils provides a magnetic gradient of 6 G/cm and three pairs of Helmholtz coils provide the fine tuning of the magnetic environment. A Coherent 899-01 Ti:Sapph laser with linewidth better than 100 kHz provides three pairs of MOT trapping beams with intensity of 8 mW/cm^2 , and the laser is red detuned from the $5S_{1/2}, F = 2 \rightarrow 5P_{3/2}, F = 3$ transition by approximately 20 MHz. A Toptica SC110 laser provides the repumper beam with intensity of 3 mW/cm^2 and it is on resonance with the transition $5S_{1/2}, F = 1 \rightarrow 5P_{3/2}, F = 2$. We capture about 10^5 atoms in the MOT with diameter of $600 \mu\text{m}$ and peak density of around 10^9 cm^{-3} . We use two CCD cameras with 10X Computar Macro Zoom lenses to monitor the fluorescence of the MOT in two perpendicular directions.

We list the relevant energy levels of ^{87}Rb for this experiment in Fig. 3.6. We

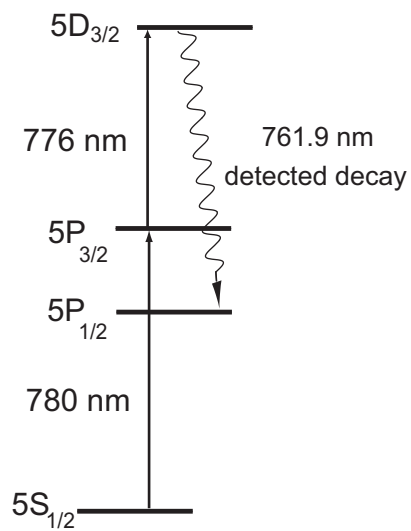


Figure 3.6: Energy levels involved in the measurement of the lifetime of the $5D_{3/2}$ state of rubidium. Trapping and cooling lasers are not shown. Energy spacings not drawn to scale.

use a two-step transition to reach the $5D_{3/2}$ state, where the trapping beam of the MOT is the first step and the $5P_{3/2}, F = 3$ state is the intermediate state. A SDL TC40-D laser with linewidth of 5 MHz provides the probe beam to reach the $5D_{3/2}$ state. We send the probe beam to the MOT region through a single mode fiber, which sets the waist ($1/e^2$ power) to 1.2 mm. The power of the probe beam is 1.0 mW for the excitation to the $5D_{3/2}, F = 3$ state.

We lock the frequency of the trapping beam using the Pound-Drever-Hall method with saturation spectroscopy of a rubidium cell. We send part of the frequency modulated light employed on this lock to an independent rubidium glass cell, where this light overlaps with that from the probe beam. We monitor the absorption of the 780 nm light, and the intermodulation of the sidebands yields error-signal like features that we use to lock the frequency of the probe beam on resonance [77, 78]. See the Appendix for further explanation.

We use a cycle of 10 μ s, and employ two different schemes for photon detection and time control for the measurement. We place a 760 nm interference filter with bandwidth of 10 nm from Andover (model 760FS10-25) in front of the detector, a Hamamatsu R636 PMT with quantum efficiency of 10% at this wavelength. Since a lot of 780 nm photons from the scattered trapping beam pass through the filter, we turn the trapping beam off after the excitation phase to decrease the background. We use two AOM's to turn on and off the trapping beam and the probe beam.

We use a 10X Computar Macro Zoom lense in front of the PMT to collect the fluorescence. Two synchronized Stanford Research pulse generators (model DG535), which have a 5 ps delay resolution and 50 ps *rms* jitter, provide all the time references

in the signal process. We amplify the pulse from the PMT's before processing them. We amplify the signal 64 times using an EG&G AN106/n plus an AN101/n DC amplifier. The output goes through an Ortec CFD (model 583) and a Lecroy level translator (model 7126). The later converts the input signal to ECL, TTL and NIM outputs. The output of the NIM signal is directed to a Stanford Research multi-channel scaler (model SR430) to monitor the photon counting histogram during the experiment. We send the ECL signal as a start pulse to a Lecroy time-to-digital converter (TDC) (model 3377), which has a resolution of 0.5 ns and is triggered by the falling edge of the input pulse. The TDC measures the delay between the observed photon and the fixed pulse given by the pulse generator. The output of the TDC goes to a Lecroy memory (model 4302) and we read out the results through a Lecroy GPIB interface (model 8901A).

3.4 Experimental results and systematics

During experimental runs, data are accumulated for a period of time from 20 and 40 minutes. With the data we build a histogram that corresponds to a decay of the fluorescence of the atomic sample for about five lifetimes. As mentioned before, the rate of detection of the fluorescence is kept low to try to minimize saturation effects such as the preferential counting of earlier events (pile-up correction) on the electronics. We perform a series of systematic studies to find any dependence of the lifetimes on the experimental parameters.

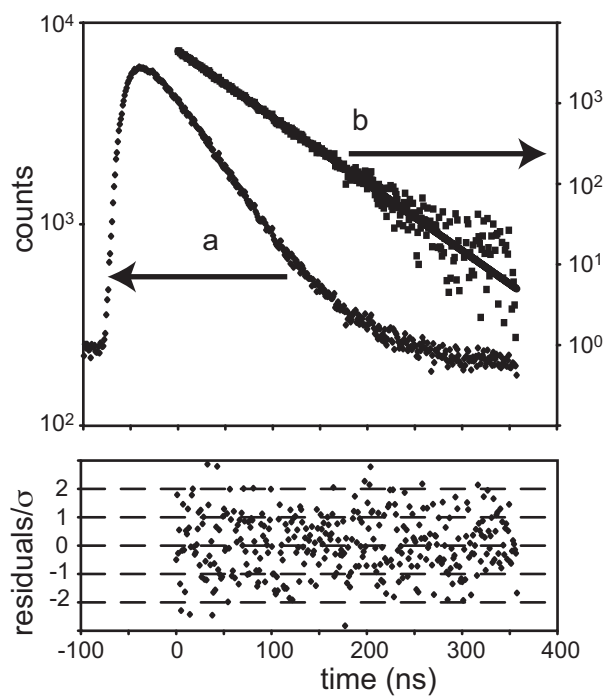


Figure 3.7: a) Raw data from the fluorescence of the francium $8s$ level. b) Experimental data with background and $7P_{3/2}$ exponential subtracted. The reduced χ^2 for this data is 1.11.

3.4.1 $8s$ state in francium

We take sets of data for about 1500 s which are individually processed and fitted. We use ORIGINTM non-linear fit package to extract the lifetime of the $8S_{1/2}$ level. ORIGINTM uses a Levenberg-Marquardt algorithm to minimize the residuals given a specified error, which in this case is Poissonian. The total number of counts in a set is typically in the order of 3×10^5 . Fig. 3.7 a) shows an example of decaying fluorescence at 718 nm resulting from the cascade decay $8S_{1/2} \rightarrow 7P_{3/2} \rightarrow 7S_{1/2}$ of francium. The observed decay signal is a sum of exponentials and a background with a slope

$$S(t) = A_{8s}e^{-t/\tau_{8s}} + A_{7p}e^{-t/\tau_{7p}} + B + Ct, \quad (3.2)$$

where τ_{8s} is the lifetime of the $8S_{1/2}$ state and τ_{7p} is the lifetime of the $7P_{3/2}$ state. The background fluorescence ($B + Ct$) comes from a remnant of 718 nm trapping light. A_{8s} and A_{7p} are the amplitudes of the decaying exponentials.

3.4.1.1 Systematics

We study the contributions of several systematic effects that can influence the measurement. These include:

A) *Truncation error*. We change the starting and end points that we use in the fit to our model to look for an effect. We do not observe any dependence beyond the statistical uncertainty.

B) *Time calibration*. The time calibration of the pulse detection system contributes 0.01% to the uncertainty.

Source	Correction [%]	Error [%]
Time calibration		± 0.01
Bayesian error		± 0.15
Pulse pile-up correction	+0.01	
TAC/MCA response nonuniformity		± 0.11
Radiation trapping		± 0.01
Imperfect laser turnoff		± 0.07
Magnetic field		± 0.11
Background slope		± 0.36
PMT response		± 0.24
Statistical		± 0.65
Total		± 0.82

Table 3.1: Error budget of the measurement of the lifetime of the $8S_{1/2}$ state of francium.

C) *Bayesian error.* We use the lifetime of the $7P_{3/2}$ level of francium to extract the lifetime of the $8S_{1/2}$. The uncertainty of the former propagates and sets an error on the lifetime of the $8s$ level. This is the bayesian error and amounts to 0.15%.

D) *TAC/MCA response nonuniformity.* The TAC and MCA nonuniformities contribute 0.11% error

E) *Radiation trapping.* There can be collisional quenching or radiation trapping (reabsorption and reemission of light due to high atomic density) that can modify

the lifetime. From our work in the equivalent state in rubidium [53] we set an upper limit to the uncertainty due to this effect of 0.01%.

F) *Imperfect laser turnoff*. We look for an effect from imperfect lasers turn off by leaving the 817 nm light on continuously. The change in the lifetime with the first-step light off or continuously on during the decay constraints the uncertainty from imperfect lasers turn off to 0.07%.

G) *Magnetic field*. We have performed an extensive search for some additional magnetic sensitivity: there is no change in the lifetime beyond the statistical uncertainty when we change the gradient of the Fr MOT. We establish a limit on magnetic field effects of 0.11%.

H) *Background slope*. The slope in the fitting function influences the value of the obtained lifetime by less than 1%. We analyze files with and without the atomic decay but always with the trap light and they give a consistent slope. We compare the lifetime obtained by leaving the slope as a free parameter or by fixing it to the background files value and obtain an uncertainty contribution of 0.36%.

I) *PMT response*. The PMT is continuously on and detects light from both the two-step excitation and the fluorescence light from the MOT. We bound the possible saturation effects on the PMT by comparing its average response in photon counting mode with the response of a fast photodiode not subject to saturation. We find a maximum contribution of 0.24%.

K) *Power of 817 nm laser*. We vary the power of the first-step laser at 817 nm and we observe no change in the measured lifetime.

L) *Pile-up correction*. We apply a pileup correction that accounts for the preferen-

tial counting of early events. We collect data with a small number of fluorescence photons to keep the corrections small. We typically count one photon every 500 cycles. The correction alters the fitted lifetime by +0.1%

We obtain an averaged χ^2 for all our data points of 1.07 ± 0.07 . Table 3.1 contains the error budget. We conclude, to the best of our knowledge, that we are limited by statistical uncertainty. We obtain a lifetime of 53.30 ± 0.44 ns for the $8S_{1/2}$ state of francium.

3.4.2 $5D_{3/2}$ state of rubidium

We record the decaying fluorescence at 761.2 nm of the $5D_{3/2}$ state until the peak count reaches 1000. Fig. 3.8 shows a typical data set with the fit and residuals. We take an additional data set of background for roughly the same time to subtract from the raw data. We fit the data to

$$y = A_{5D_{3/2}} e^{-t/\tau_{5D_{3/2}}} + F, \quad (3.3)$$

where $\tau_{5D_{3/2}}$ is the lifetime of the $5D_{3/2}$ state. The constants multiplying the exponential, $A_{5D_{3/2}}$ corresponds to the amplitude and F to the background. We use the Levenberg-Marquardt algorithm [76] to fit the data to the corresponding signal and extract the desired lifetime.

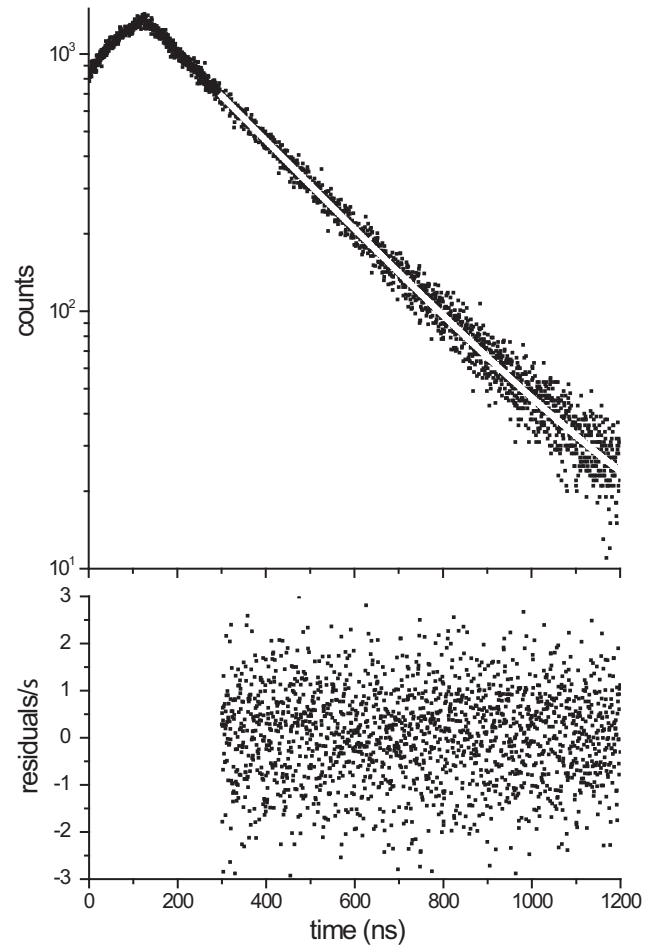


Figure 3.8: Decay of the fluorescence of the $5D_{3/2}$ state of rubidium with residuals and best fit.

3.4.2.1 Systematics

Rubidium atoms might be sensitive to the same type of effects as francium atoms. We search for possible systematic errors in both measurements. Table 3.2 presents the error budget [65].

In addition to the above mentioned systematics, we look for quantum beats in our data. Quantum beats come from the interference of the decay paths from several coherently excited states to the same lower state. We search for quantum beats arising from interference of hyperfine states ($5D_{3/2}, F = 3$ and $5D_{3/2}, F = 4$) ≈ 40 MHz apart. The FFT of the 776 nm laser pulse shows a very small component at this frequency (1/200 of the total power) which reduces the probability of a coherent excitation. A similar analysis of the residuals shows no indication of a component at this frequency. We search also for quantum beats arising from Zeeman structure. See Ref. [65] for a detailed discussion. We put a limit on the possible influence of quantum beats of 0.15%.

3.5 Comparison with theory

Table 3.3 compares the experimental value obtained in this work of the lifetime of the $8S_{1/2}$ state of francium with the theoretical predictions of *ab initio* calculations from different groups [34, 69, 79, 80]. The theoretical results, albeit somewhat dispersed, are in excellent agreement (within 1 %) with the experimental value.

Table 3.4 shows the experimental results of the lifetime of the $5D_{3/2}$ state of rubidium as well as the theoretical predictions of Refs. [72, 81]. Previous experi-

Source	Correction [%]	Error [%]
Statistical		± 0.25
Time calibration		$< \pm 0.01$
TDC nonuniformity		± 0.01
Pulse Pileup	-0.1	
Quantum beats and magnetic field		$< \pm 0.16$
Radiation trapping		$< \pm 0.10$
Other Systematics		$< \pm 0.6$
Total		± 0.66

Table 3.2: Error budget of the measurement of the $5D_{3/2}$ state lifetime of rubidium.

Table 3.3: Comparison of the measured lifetime of the $8S_{1/2}$ state of francium with *ab initio* calculations.

		$\tau_{8S_{1/2}}$ [ns]
Experiment	This work	53.30 ± 0.44
Theory	Dzuba <i>et al.</i> [69]	53.0
	Dzuba <i>et al.</i> [79]	53.6
	Safronova <i>et al.</i> [34]	53.4
	Johnson <i>et al.</i> [80]	53.8

Table 3.4: Comparison of the measured lifetime of the $5D_{3/2}$ state of rubidium with previous work and calculations.

		$\tau_{5D_{3/2}}$ [ns]
Experiment	This work	243.6 ± 1.6
	Tai <i>et al.</i> [73]	205 ± 40
Theory	Theodosiou [81]	240
	Safronova <i>et al.</i> [72]	243

mental results are also included in the table. The theoretical predictions of Ref. [72] are in good agreement with our experimental results since the estimated theoretical error for d states is 5% due to the high correlation effects between electrons in the calculations [82].

3.6 Conclusions

We have measured the lifetime of the $8S_{1/2}$ state of francium to a precision of 0.8% with a value of $\tau_{8S_{1/2}} = 53.5 \pm 0.44$ ns [14]. This result is in excellent agreement with the *ab initio* calculations from several groups [34, 69, 79, 80] (see Table 3.3) .

We have measured also the lifetime of the $5D_{3/2}$ state in rubidium obtaining $\tau_{5D_{3/2}} = 246.3 \pm 1.6$ ns [65]. Our result has enough precision to confirm the improvement of the scaled all-order method [72] (see Table 3.4).

Our measurements establish the reliability of the MBPT calculations of matrix

elements that contribute to the total lifetime of the state. They take into account the relativistic effects present in the atoms as well as the multiple correlations. Their accuracy is vital for future interpretations of PNC measurements.

Chapter 4

Conclusions and outlook

The work in this thesis stands as the latest stepping stone in the effort towards the measurement of the nuclear anapole moment in several isotopes of francium and concludes the precision lifetime measurements of the lowest energy levels of francium. The precision achieved in the measurement is a consequence of the high efficiency trap for francium [8] and the intensive analogous work done in the $6S_{1/2}$ level of rubidium [53]. The value we obtain is in excellent agreement (within 1%) with the *ab initio* calculations of several groups [34, 69, 79, 80].

The measurement of the lifetime of the $8S_{1/2}$ state also marks the conclusion of a chapter in the work of our collaboration. Having demonstrated that high precision studies of atomic properties in several isotopes of francium are feasible, our efforts were directed towards the design and test of the new science chamber where the experiment will take place. The science chamber, which is being tested at the University of Maryland, is currently under vacuum with a pressure better than 10^{-10} torr. We have demonstrated the transfer of ^{87}Rb atoms from a mock-up version of the dry film coated glass cell used to trap francium across 70 cm with an efficiency better than 50%.

These results are encouraging, however, there is still work ahead of us. The understanding and control of the electromagnetic environment observed by the fran-

Francium atoms inside the far off-resonance dipole trap stands as one of the issues to be solved. A viable option consists of loading the cold francium atoms into a blue detuned dipole trap. The dipole trap can be created with a two-dimensional AOM that generates a “dark” region where the atoms will reside [83], although this is not the only option [84]. Once loaded, careful interrogation of the atomic cloud is needed to estimate the properties of the electromagnetic environment in this region of space.

We have also advanced the development of the microwave Fabry-Perot cavity that will drive the parity-forbidden $E1$ transition. We have demonstrated, in a confocal configuration, that a high Q is achievable at the frequency corresponding to the hyperfine splitting of ^{210}Fr (8300 at 46.21 GHz). We have succeeded in generating an error signal to lock the microwave cavity on resonance [85]. The microwave mirrors (glass mirrors coated with a 3 μm layer of copper and a 1 μm layer of gold with a diameter of 7.5 cm and a radius of curvature of 14 cm) are lightweight and vacuum compatible. Further work should be focused on the support system that will hold and stabilize them inside the science chamber and the non-trivial connection through ultra-high vacuum of U band electromagnetic waves.

The measurements of atomic properties of francium as well as the R&D work for the measurement of the anapole moment is perfectly complemented by our work in rubidium. As mentioned earlier on, the crucial systematic studies inherent in all precision measurement work can be extensively analyzed in either isotope of rubidium and then extrapolated to francium. The current experimental exploration and test of the techniques that will be used in final measurement continue to be

Property	Atom	Level	Value
Hyperfine separation	^{87}Rb	$6S_{1/2}$	1615.32 ± 0.16 MHz
Hyperfine separation	^{85}Rb	$6S_{1/2}$	807.66 ± 0.08 MHz
Hyperfine anomaly difference	^{85}Rb and ^{87}Rb	$6S_{1/2}$	-0.0036(2)
Lifetime	^{87}Rb	$5D_{3/2}$	246.3 ± 1.6 ns
Lifetime	^{210}Fr	$8S_{1/2}$	53.5 ± 0.44 ns

Table 4.1: Summary of spectroscopic measurements presented in this thesis.

tested with rubidium.

Besides being our “test” atom, measurements in rubidium stand as important results in their own right. Table 4.1 shows the values of the atomic properties of rubidium presented in this thesis as well as the lifetime of the $8S_{1/2}$ state of francium. We have measured the hyperfine splittings of the $6S_{1/2}$ level of ^{87}Rb and ^{85}Rb and extracted from the measurements a hyperfine anomaly attributed to the Bohr-Weisskopf effect. Similar measurements can be performed in francium to explore the behavior of the wavefunction as a function of nuclear matter in one [44, 86] or two photon transitions and with the Fabry-Perot cavity attempt to measure ratios of g -factors of different isotopes. We have also measured and improved the lifetime of the $5D_{3/2}$ state of ^{87}Rb . Theory is in excellent agreement with our results and, in the case of the lifetime of the $5D_{3/2}$ state of rubidium, stresses the importance of correlations between electrons for the states with high angular momentum. Measurements in rubidium are and will continue to be an important component in our work.

Appendix A

Two-photon lock.

A.1 Introduction

Saturation spectroscopy is a reliable and convenient way to resolve closely spaced energy levels immersed in a Doppler broadened medium. Other techniques exist that reduce or eliminate the first order Doppler shift atoms experience as they move away or towards a laser beam, among them laser cooling and atomic beam spectroscopy. Saturation spectroscopy remains the simplest to implement and is still routinely used in laboratories all around the world to perform basic science [23, 87] as well as for applications closer to its origins such as frequency locking of lasers frequencies to atomic resonances.

Saturation spectroscopy, in its most basic form, has two lasers (pump and probe) interacting with an atomic vapour at a finite temperature. The Doppler velocity distribution of the sample changes due to the non-linear interaction of both lasers with the medium. The pump laser, with a higher intensity than the probe, saturates the atoms of a velocity group inhibiting them from absorbing the weaker probe beam. The absorption of the probe presents sub-Doppler peaks on top of a Doppler profile corresponding to the atomic resonances with shapes and heights that depend on the polarization of the beams and their relative intensities [88, 89].

The lasers excite the sample starting from ground state. This has the advan-

tage that, within reasonable laser intensities, the ground state is always populated guaranteeing a good signal to noise ratio since the absorption of the laser depends on the number of atoms in the ground state. However, this method is no longer adequate when we want to replace one of the laser beams with a beam of a different color to explore higher excited levels using two-step transitions. One has to work hard to detect changes of absorption of the probe beam plus the added complication that detectors at the required frequency might not be readily available.

Two-color saturation spectroscopy is a method to detect small changes in the population of the ground state due to transfer to higher excited states. The technique overcomes the two main inconveniences of direct absorption of the probing laser. Extensions of the technique can be used to explore well known phenomena observed in lambda-type systems such as electromagnetically induced transparency (EIT) in ladder type systems and other coherent behavior of atomic systems like electromagnetically induced absorption (EIA). This has been demonstrated recently by Becerra *et al.* in a two-photon Dichroic Atomic Vapor Laser Lock (T-P DAVLL) to stabilize the frequency of a laser [90]. Sheludko *et al.* have found further use for the technique in state selective imaging in a MOT [91].

We use the $5S_{1/2} \rightarrow 5P_{3/2} \rightarrow 5D_{5/2}$ ladder transition in ^{87}Rb to illustrate the main features of the technique. To further show the reliability of the method we employ the absorption spectrum to lock the frequency of a laser to the $5P_{3/2} \rightarrow 5D_{5/2}$ excited atomic resonance. We accomplish this without modulating the locked laser. This is very worthwhile because the electronic modulation of the laser itself can carry unwanted effects such as sidebands at high or lower frequencies as well as

bandwidth problems. The method is not limited to this set and can be extended to other atomic levels [78, 92].

Our experimental setup consists of two counter-propagating lasers overlapped inside a glass cell filled with natural isotopic abundances of rubidium at room temperature. The pump laser and first step of the transition at 780 nm is locked on resonance to the $F = 4$ hyperfine state of the $5P_{3/2}$ level of ^{87}Rb . A small bandwidth EOM at ≈ 15 MHz modulates its frequency. The probe laser and second step of the transition at 776 nm scans over the $5D_{5/2}$ hyperfine manifold. Fig. A.1 (a) shows our atomic system and corresponding lasers. We monitor the absorption of the pump laser after it propagates through the glass cell as a function of the detuning of the probe laser with a fast photodiode. The signal has a slowly varying (DC) and a fast varying (AC) component. The AC component is demodulated and stored along with the DC part.

The organization of the Appendix is as follows: section A.2 contains the theoretical model, section A.3 explains the experimental setup and method, and section A.4 has the conclusions.

A.2 Theoretical model

We present a theoretical model using a density matrix formalism to understand the experimental absorption spectra. We propose a three level system in a ladder configuration interacting with two lasers, one of which has frequency modulated (FM) sidebands (see Fig. A.1 (b)), to describe the slowly and varying components

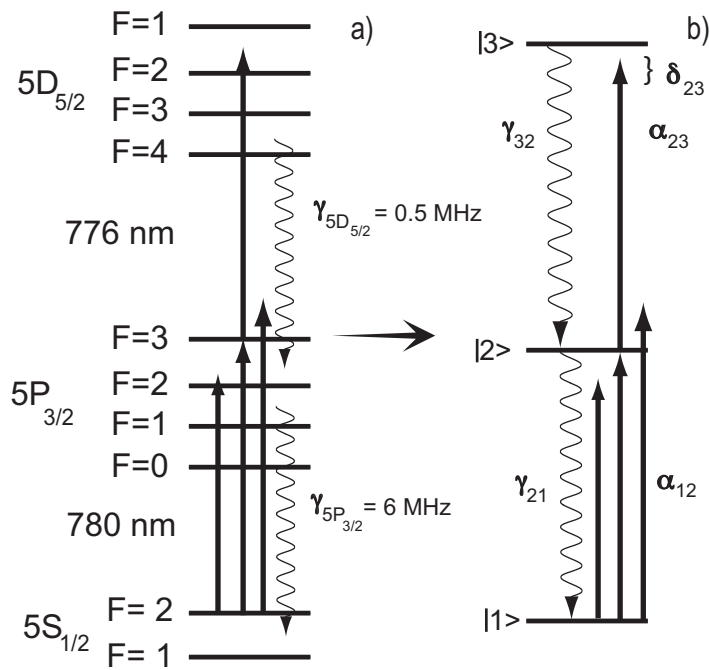


Figure A.1: a) Relevant atomic energy levels for the experiment with corresponding lasers. The longer and shorter arrows besides the medium size arrow in the first step represent the sidebands of the carrier. b) Simplified atomic model. Energy spacings not drawn to scale.

of the absorption. This approach, as opposed to just treating the three-level system with two lasers, has the advantage that we are able to describe both AC and DC and the simpler system by setting the modulation index to zero.

Two-step excitations represent a challenge to the atomic physicist. The system is seldom described by a three-level closed atomic system. The electron at the last stage of the excitation sees a plethora of decay channels, and do not necessarily return to the starting point *i.e.* optical pumping effects play a major role in determining the atomic behavior [63]. The $5S_{1/2} \rightarrow 5P_{3/2} \rightarrow 5D_{5/2}$ ladder system (see Fig. A.1 (a)), however, is appropriate since the atomic physics of the system conspires to make it almost a closed system [25]. In addition, the almost perfect Doppler cancelation of the counter propagating configuration motivates us to model the system as Doppler free. To keep the system tractable we ignore the Zeeman sublevels of the system.

Level $|1\rangle$ in Fig. A.1 (b) represents the higher hyperfine state of the $5S_{1/2}$ level ($F = 2$) while $|2\rangle$ is the highest hyperfine state of the $5P_{3/2}$ level ($F = 3$) of ^{87}Rb . The decay rate between the two levels is $\gamma_{21}/2\pi = 6$ MHz [52]. We simplify the hyperfine states of the $5D_{5/2}$ level to just one level with decay rate $\gamma_{32}/2\pi = 0.5$ MHz [65]. The ground and intermediate levels are coupled by three lasers: a carrier and two sidebands separated from the carrier by Δ (in MHz). We represent the amplitude of the carrier by a Rabi frequency α_{12} and the sidebands by a modulation depth β . The intermediate and the excited levels are coupled by α_{23} . The detuning of the carrier between levels $|1\rangle$ and $|2\rangle$ is zero for our experiment and we let the detuning between levels $|2\rangle$ and $|3\rangle$ vary as δ_{23} . The total population is

normalized to one.

We have a set of nine linear equations for the slowly varying elements of the density matrix σ_{nm} after using the rotating wave approximation with the sidebands rotating, one clockwise, one counter clockwise, at a frequency Δ . The equations are:

$$\begin{aligned} & \sum_k (\gamma_{kn} \sigma_{kk} - \gamma_{nk} \sigma_{nn}) + \\ & \frac{i}{2} \sum_k (\alpha_{nk} \sigma_{kn} - \sigma_{nk} \alpha_{kn}) = \dot{\sigma}_{nm} \text{ for } n = m, \\ & [i(\Omega_{nm} - \omega_{nm}) - \Gamma_{nm}] \sigma_{nm} + \\ & \frac{i}{2} \sum_k (\alpha_{nk} \sigma_{km} - \sigma_{nk} \alpha_{km}) = \dot{\sigma}_{nm} \text{ for } n \neq m, \end{aligned}$$

where $\omega_{nm} = (E_n - E_m)/\hbar$ is the transition frequency, and $\Omega_{nm} = -\Omega_{mn}$ is the laser frequency connecting the levels. The damping rate is given by:

$$\Gamma_{nm} = \frac{1}{2} \sum_k (\gamma_{nk} + \gamma_{mk}),$$

and $\alpha_{12} = \alpha_{12}^0 (1 + \beta e^{i\Delta t} - \beta e^{-i\Delta t})$. Time dependence of the Rabi frequency makes the standard approach for obtaining the steady state solution of the system not feasible. Instead, we use a Floquet basis expansion of the density matrix [93] to solve the system of equations. We replace each of the slowly rotating elements of the density matrix by:

$$\sigma_{nm}(t) = \sum_{k=-p}^p \sigma_{nm}^{(k)} e^{ik\Delta t},$$

where $\sigma_{nm}^{(k)}$ is the Fourier amplitude of the component oscillating at $k\Delta t$. The system is now a series of $2p + 1$ coupled equations for some large p that have to be solved

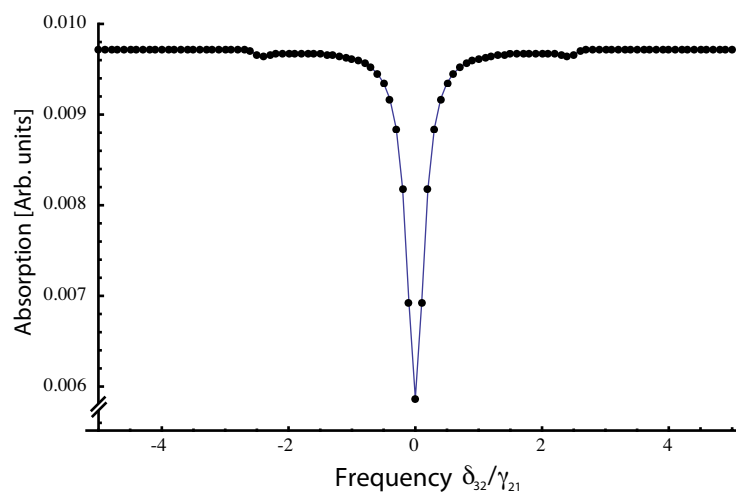


Figure A.2: Numerical simulation of the absorption of the 780 nm laser as a function of the normalized detuning of the 776 nm laser in units of γ_{21} . The parameters are : $\beta = 1/10$, $\alpha_{12}^0 = 1/100$, $\alpha_{23} = 1/4$, $\gamma_{32} = 1/10$, and $\Delta = 2.5$

recursively. It is necessary to set $\sigma^{(k)nm} = 0$ for some p to cut off the infinite number of coupled equations. By solving the $p - 1$ and the $-(p - 1)$ equations in terms of their predecessors we can extract $\sigma_{12}^{(p)}$. For our experiment we are interested in the terms $\sigma_{12}^{(0)}$, $\sigma_{12}^{(-1)}$, and $\sigma_{12}^{(1)}$ which are proportional to the absorption of the first laser carrier and sidebands, respectively. We plot the absolute value of the imaginary part as a function of δ_{23} to recover the DC component of the absorption. This is necessary to take into account the square-law nature of the photodiode. Our three level model reproduces the resonance features of the absorption observed as the second excitation goes into resonance as well as the error-signal like features once the absorption is demodulated, Fig A.2 and A.3, respectively.

A.3 Apparatus and method

Figure A.4 presents a block diagram of our experimental setup. The pump laser is a Coherent 899-01 Ti:sapphire laser with a linewidth of less than 100 kHz. We frequency modulate the pump laser at ≈ 15 MHz by a small bandwidth EOM. A small amount of laser power gets redirected to a glass cell filled with rubidium at room temperature to lock the laser frequency to the $5P_{3/2}$ crossover line of the $F = 2$ and $F = 4$ hyperfine levels.

The main beam at 780 nm goes through an AOM set at 106 MHz in double-pass configuration to set it on resonance to the $F = 4$ hyperfine level. The probe laser is an SDL diode laser with a linewidth of 5 MHz at 776 nm. The lasers overlap inside an independent rubidium glass cell at room temperature wrapped

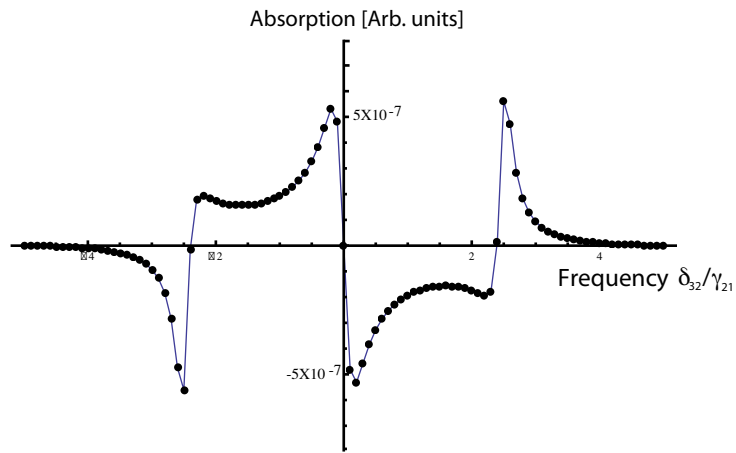


Figure A.3: Numerical simulation of the demodulated absorption of the pump laser as a function of the normalized detuning of the probe laser in units of γ_{21} . The parameters are : $\beta = 1/10$, $\alpha_{12}^0 = 1/100$, $\alpha_{23} = 1/4$, $\gamma = 1/10$, and $\Delta = 2.5$

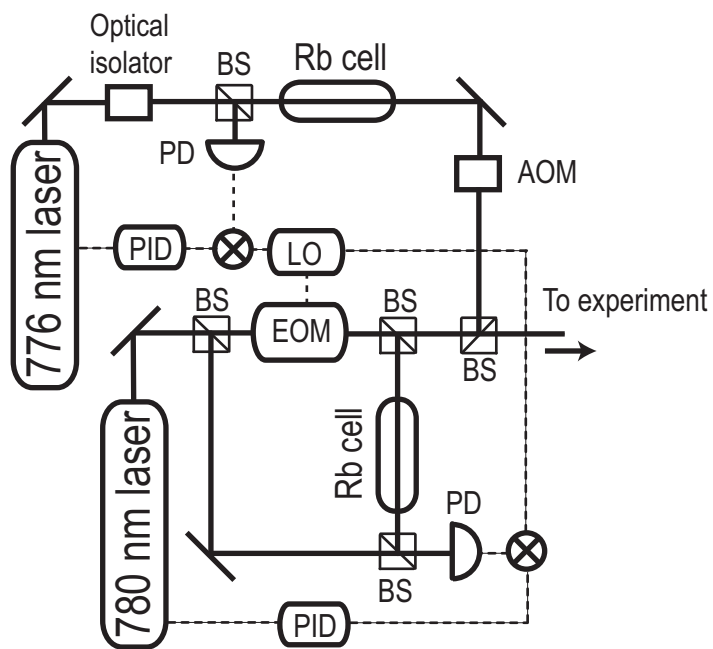


Figure A.4: Block diagram of the experiment. Key for the figure PD: photodiode, LO: local oscillator, BS: beam splitter, PID: proportional-integral-differential controller.

in μ -metal in lin-perp-lin polarization configuration. Their $1/e^2$ power diameter is 1 mm. We scan the probe laser over the $5D_{5/2}$ level hyperfine manifold and observe the absorption of the pump laser as a function of the probe laser detuning using a fast photodetector. We send the signal to a bias-T and record the DC and demodulated AC components with a Lecroy WaveSurfer digital oscilloscope with an 8-bit resolution.

We keep the power of the pump laser and the modulation depth fixed to a value of 100 μ W and $\beta = 0.1$, respectively. We change the power of the probe beam and observe its influence on the spectra. It is possible to observe the resonant features of the $5D_{5/2}$ hyperfine manifold with little as 100 μ W of probe power. Higher probe power increases the signal size and the width of the features. Varying the polarization and powers allows us to observe narrow features coming from electromagnetically-induced transparency (EIT) [56]. We restrict ourselves to a parameter region where these very narrow features are absent.

Figure A.5 and A.6 show typical experimental traces of the absorption of the 780 nm laser. The spectrum has been offset to zero transmission for convenience. The first of these, Fig. A.5, has the DC component of the absorption with the sidebands appearing on both sides of the main resonances. No Doppler background is observed for any of the experimental conditions explored. Fig. A.6 (a) shows the lower hyperfine states of the $5D_{5/2}$ level manifold with no sidebands for clarity. Fig. 6 (b) has the demodulated AC component of the absorption. The dashed lines identify the error-like features with their corresponding hyperfine levels. We use this spectrum to stabilize the frequency of the probe laser.

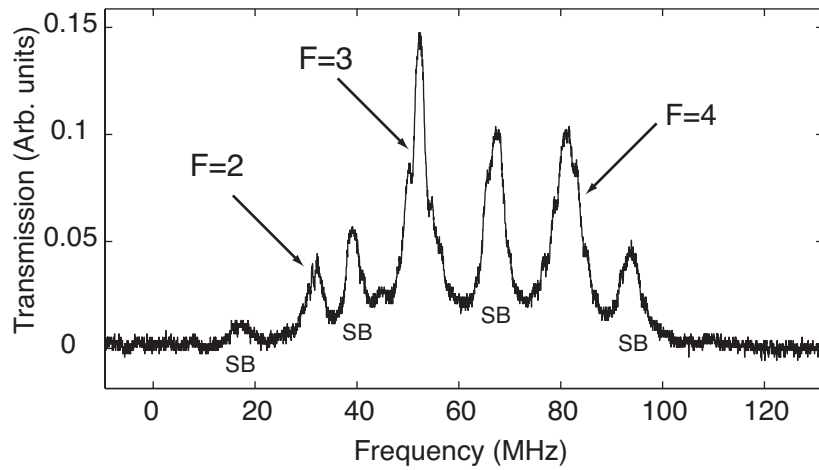


Figure A.5: DC component of the absorption of the 780 nm laser as a function of the probe laser detuning showing main resonances as well as sidebands (SB). The power of the probe and pump beam are 4.3 mW and 100 μ W, respectively.

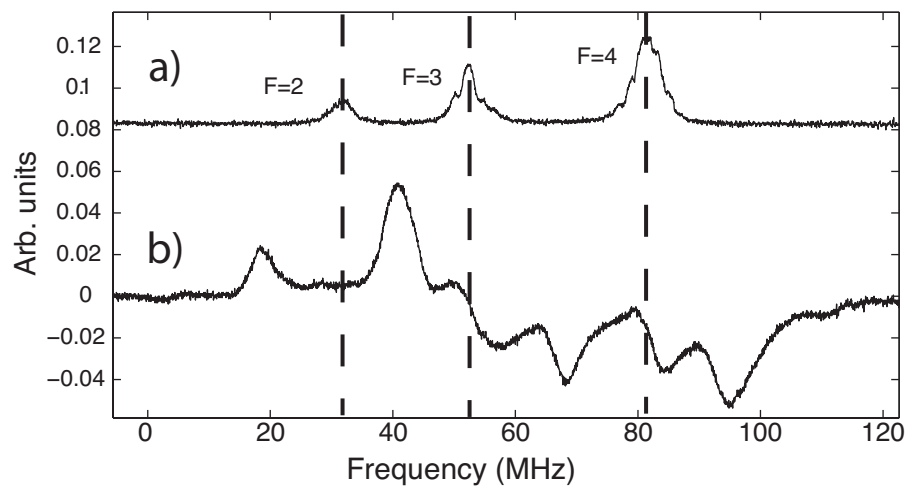


Figure A.6: Experimental traces of (a) absorption without sidebands and (b) demodulated absorption of 780 nm laser as a function of detuning of the 776 nm laser. The power of the probe and pump beam are 4.3 mW and 100 μ W, respectively.

To test our lock we monitor the laser frequency of the probe beam using a Coherent confocal Fabry-Perot cavity with a free spectral range of 1.5 GHz. Fig. A.7 shows the fringe-side transmission of the probe laser through the cavity. We monitor the behavior of the laser before and after it has been locked. The reduction of the frequency excursions is quite evident as the laser is locked to the atomic resonance. Under normal experimental conditions we have observed locking times of 30 minutes.

A.4 Conclusions

We have presented two-color saturation spectroscopy as a reliable and simple method to detect transfer of population from the ground state to higher excited states in two-photon transitions. The method is ideal for studies of properties of excited states of atoms, such as measurements of hyperfine splittings [64] and lifetimes [65]. The resulting two-photon spectrum has a high enough signal to noise ratio to generate error-like features to lock the frequency of a laser to an atomic transition that is not connected to the ground state [77].

The measurement of the absorption of the pump beam presents several advantages. First of all, the absorption spectra do not present a Doppler background due to the lack of an equilibrium thermal population in the intermediate state. Second, the absorption of the pump beam (or lack thereof) is always guaranteed since a large number of atoms are always in the ground state and even small changes *i.e.* excitation to the last step of the transition, will be noticeable even for small powers of the

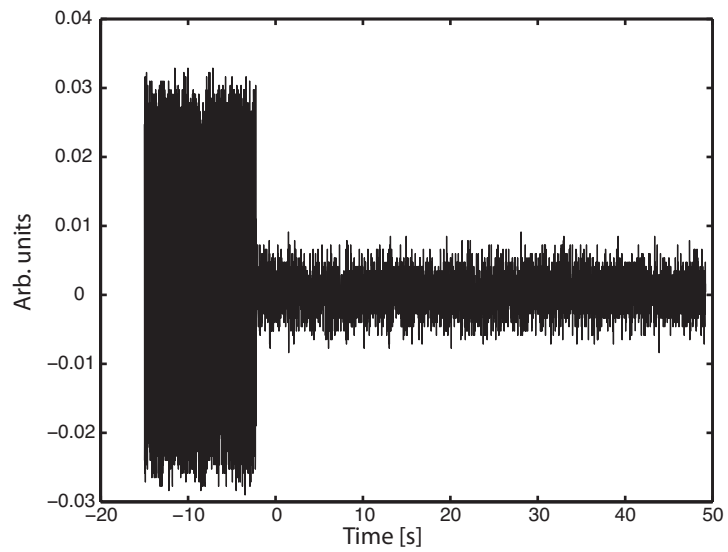


Figure A.7: Fringe-side transmission of the SDL laser at 776 nm through a confocal Fabry-Perot cavity. The reduction of the amplitude of the signal corresponds to the locking of the laser to the $5P_{3/2} \rightarrow 5D_{5/2}$ excited atomic transition.

pump beam. We hope that the method will stimulate studies of atomic properties of excited states and further push the experimental precision and theoretical work in excited atomic states.

Bibliography

- [1] E. Gomez, L. A. Orozco, and G. D. Sprouse, Rep. Prog. Phys. **66**, 79 (2006).
- [2] E. Gomez, S. Aubin, G. D. Sprouse, L. A. Orozco, and D. P. DeMille, Phys. Rev. A **75**, 033418 (2007).
- [3] M. A. Bouchiat, Phys. Rev. Lett. **100**, 123003 (2008).
- [4] H. J. Metcalf and P. van der Straten, *Laser Cooling and Trapping* (Springer-Verlag, New York, 1999).
- [5] C. S. Wood, S. C. Bennett, D. Cho, B. P. Masterson, J. L. Roberts, C. E. Tanner, and C. E. Wieman, Science **275**, 1759 (1997).
- [6] C. S. Wood, S. C. Bennett, J. L. Roberts, D. Cho, and C. E. Wieman, Can. J. Phys. **77**, 7 (1999).
- [7] J. E. Simsarian, A. Ghosh, G. Gwinner, L. A. Orozco, G. D. Sprouse, and P. A. Voytas, Phys. Rev. Lett. **76**, 3522 (1996).
- [8] S. Aubin, E. Gomez, L. A. Orozco, and G. D. Sprouse, Rev. Sci. Instrum. **74**, 4342 (2003).
- [9] J. E. Simsarian, W. Shi, L. A. Orozco, G. D. Sprouse, and W. Z. Zhao, Opt. Lett. **21**, 1939 (1996).
- [10] W. Z. Zhao, J. E. Simsarian, L. A. Orozco, W. Shi, and G. D. Sprouse, Phys. Rev. Lett. **78**, 4169 (1997).
- [11] J. M. Grossman, R. P. Filler III, T. E. Mehlstäubler, L. A. Orozco, M. R. Pearson, G. D. Sprouse, and W. Z. Zhao, Phys. Rev. A **62**, 052507 (2000).
- [12] J. M. Grossman, R. P. Filler III, L. A. Orozco, M. R. Pearson, and G. D. Sprouse, Phys. Rev. A **62**, 062502 (2000).
- [13] S. Aubin, E. Gomez, L. A. Orozco, and G. D. Sprouse, Phys. Rev. A **70**, 042504 (2004).
- [14] E. Gómez, L. A. Orozco, A. Pérez Galván, and G. D. Sprouse, Phys. Rev. A **71**, 062504 (2005).

- [15] Y. B. Zel'dovich, *Sov. Phys.-JETP* **6**, 1184 (1958).
- [16] I. B. Khriplovich, *Parity Non-Conservation in Atomic Phenomena* (Gordon and Breach, New York, 1991).
- [17] V. V. Flambaum and D. W. Murray, *Phys. Rev. C* **56**, 1641 (1997).
- [18] V. V. Flambaum, I. B. Khriplovich, and O. P. Sushkov, *Phys. Lett. B* **146**, 367 (1984).
- [19] W. M. Itano, J. C. Begquist, J. J. Bollinger, J. M. Gilligan, D. J. Heinzen, F. L. Moore, M. G. Raizen, and D. J. Wineland, *Phys. Rev. A* **47**, 3554 (1993).
- [20] E. Gomez, personal communication.
- [21] J. Dalibard, personal communication.
- [22] G. P. Barwood, P. Gill, and W. R. C. Rowley, *Appl. Phys. B: Photophys. Laser Chem.* **53**, 142 (1991).
- [23] J. Ye, S. Swartz, P. Jungner, and J. L. Hall, *Opt. Lett.* **21**, 1280 (1996).
- [24] V. Gerginov, A. Derevianko, and C. E. Tanner, *Phys. Rev. Lett.* **91**, 072501(2003).
- [25] A. Marian, M. C. Stowe, J. R. Lawall, D. Felinto, and J. Ye, *Science* **306**, 2063 (2004).
- [26] E. Gómez, S. Aubin, L. A. Orozco, and G. D. Sprouse, *J. Opt. Soc. Am. B* **21**, 2058 (2004).
- [27] H.-C. Chui, M.-S. Ko, Y.-W. Liu, J.-T. Shy, J.-L. Peng, and H. Ahn, *Opt. Lett.* **30**, 842 (2005).
- [28] S. C. Bennett and C. E. Wieman, *Phys. Rev. Lett.* **82**, 2484 (1999).
- [29] S. C. Bennett and C. E. Wieman, *Phys. Rev. Lett.* **83**, 889 (1999).
- [30] S. C. Bennett and C. E. Wieman, *Phys. Rev. Lett.* **82**, 4153 (1999).
- [31] A. Derevianko, personal communication.
- [32] A. Corney, *Atomic and Laser Spectroscopy* (Clarendon Press, Oxford, 1977).

- [33] H. Kopfermann, *Nuclear Moments* (Academic Press, New York, 1958).
- [34] M. S. Safronova, W. R. Johnson, and A. Derevianko, Phys. Rev. A **60**, 4476 (1999).
- [35] R. Pal, M. S. Safronova, W. R. Johnson, A. Derevianko, and S. Porsev, Phys. Rev. A **75**, 042515 (2007).
- [36] M. S. Safronova, A. Derevianko, and W. R. Johnson, Phys. Rev. A **58**, 1016 (1998).
- [37] W. R. Johnson, *Atomic Structure Theory: Lectures on Atomic Physics*, (Springer, New York, NY, 2007).
- [38] B. A. Brown, A. Derevianko, and V. V. Flambaum, arXiv:hep-ph/0804.4315v1 (2008).
- [39] J. E. Rosenthal and G. Breit, Phys. Rev. **41**, 459 (1932).
- [40] M. F. Crawford and A. L. Schawlow, Phys. Rev. **76**, 1310 (1949).
- [41] H. J. Rosenberg and H. H. Stroke, Phys. Rev. A **5**, 1992 (1972).
- [42] A. Bohr and V. F. Weisskopf, Phys. Rev. **77**, 94 (1950).
- [43] J. R. Persson, Eur. Phys. J. A **2**, 3 (1998).
- [44] J. S. Grossman, L. A. Orozco, M. R. Pearson, J. E. Simsarian, G. D. Sprouse, and W. Z. Zhao, Phys. Rev. Lett. **83**, 935 (1999).
- [45] I. Angeli, At. Data Nucl. Data Tables **87**, 185 (1999).
- [46] C. Thibault, F. Touchard, S. Büttgenbach, R. Klapisch, M. de Saint Simon, H. T. Duong, P. Jacquinet, P. Juncar, S. Liberman, P. Pillet, J. Pinard, J. L. Vialle, A. Pesnelle, and G. Huber, Phys. Rev. C **23**, 2720 (1981).
- [47] L. Armstrong, *Theory of the Hyperfine Structure of Free Atoms* (Wiley-Interscience, New York, 1971).
- [48] H. H. Stroke, R. J. Blin-Stoyle, and V. Jaccarino, Phys. Rev. **123**, 1326 (1961).
- [49] T. Yamazaki, T. Nomura, S. Nagamiya, and T. Katou, Phys. Rev. Lett. **25**, 547 (1970).

- [50] H. T. Duong, C. Ekström, M. Gustafsson, T. T. Inamura, and P. Juncar, P. Lievens, I. Lindgren, S. Matsuki, T. Murayama, R. Neugart, T. Nilsson, T. Nomura, M. Pellarin, S. Penselin, J. Persson, J. Pinard, I. Ragnarsson, O. Redi, H. H. Stroke, and J. L. Vialle, the ISOLDE Collaboration, *Nuc. Instr. and Meth. A* **325**, 465 (1993).
- [51] S. Stenholm, *Foundations of Laser Spectroscopy* (Dover Publications, Inc., Mineola, NY, 2005).
- [52] J. E. Simsarian, L. A. Orozco, G. D. Sprouse, and W. Z. Zhao, *Phys. Rev. A* **57**, 2448 (1998).
- [53] E. Gomez, F. Baumer, A. D. Lange, G. D. Sprouse, and L. A. Orozco, *Phys. Rev. A* **72**, 012502 (2005).
- [54] E. A. Burt and C. R. Ekstrom, *Rev. Sci. Instrum.* **73**, 2699 (2002).
- [55] D. Budker, D. Kimbal, and D. DeMille, *Atomic Physics. An exploration through problems and solutions.* (Oxford University Press, Oxford, 2004).
- [56] Julio Gea-Banaclache, Yong-qing Li, Shao-zheng Jin, and Min Xiao, *Phys. Rev. A* **51**, 576 (1995).
- [57] J. H. Marquardt, H. G. Robinson, and L. Hollberg, *J. Opt. Soc. Am. B* **13**, 1384 (1996)
- [58] C. Delsart and J. Keller, *J. Phys. (Paris)* **39**, 350 (1978).
- [59] N. J. Stone, *At. Data Nucl. Data Tables* **90**, 75 (2005).
- [60] R. Gupta, W. Happer, L. K. Lam, and S. Svanberg, *Phys. Rev. A* **8**, 2792 (1973).
- [61] E. Arimondo, M. Inguscio, and P. Violino, *Rev. Mod. Phys.* **49**, 31 (1977).
- [62] A. Marian, M. C. Stowe, D. Felinto, and J. Ye, *Phys. Rev. Lett.* **95**, 023001 (2005).
- [63] A. Pérez Galván, Y. Zhao, and L. A. Orozco, *Phys. Rev. A* **78**, 012502 (2008).
- [64] A. Pérez Galván, Y. Zhao, L. A. Orozco, E. Gomez, F. J. Baumer, A. D. Lange, and G. D. Sprouse, *Phys. Lett. B* **655**, 114 (2007).

- [65] D. Sheng, A Pérez Galván, and L. A. Orozco, Phys. Rev. A **78**, 062506 (2008).
- [66] J. Guéna, D. Chauvat, P. Jacquier, E. Jahier, M. Lintz, S. Sanguinetti, A. Wasan, M. A. Bouchiat, A. V. Papoyan, and D. Sarkisyan, Phys. Rev. Lett. **90**, 143001 (2003).
- [67] E. N. Fortson, Phys. Rev. Lett. **70**, 2383 (1993).
- [68] A. Kreuter, C. Becher, G. P. T. Lancaster, A. B. Mundt, C. Russo, H. Häffner, C. Roos, W. Hänsel, F. Schmidt-Kaler, R. Blatt, and M. S. Safronova, Phys. Rev. A **71**, 032504 (2005).
- [69] V. A. Dzuba, V. V. Flambaum, and J. S. M. Ginges, Phys. Rev. A **63**, 062101 (2001).
- [70] A. Steane, Appl. Phys. B **64**, 623 (1997).
- [71] H. C. Nägerl, C. Roos, D. Leibfried, H. Rohde, G. Thalhammer, J. Eschner, F. Schmidt-Kaler, and R. Blatt, Phys. Rev. A **61**, 023405 (2000).
- [72] M. S. Safronova, C. J. Williams, and C. W. Clark, Phys. Rev. A **69**, 022509 (2004).
- [73] C. Tai, W. Happer, and R. Gupta, Phys. Rev. A **12**, 736 (1975).
- [74] D. V. O'Connor and D. Phillips, *Time Correlated Single Photon Counting* (Academic Press, London, 1984).
- [75] W. Z. Zhao, J. E. Simsarian, L. A. Orozco, and G. D. Sprouse, Rev. Sci. Instrum. **69**, 3737 (1998).
- [76] W. H. Press, B. P. Flannery, S. A. Teukolsky, and W. T. Vetterling, *Numerical Recipes: The Art of Scientific Computing* (Cambridge University Press, Cambridge, 1987).
- [77] A. Pérez Galván, D. Sheng, L. A. Orozco, and Y. Zhao, arXiv:0812.1386 (2008).
- [78] R. Boucher, M. Breton, N. Cyr, and M. Têtu, IEEE Photonics Technology Letters **4**, 327 (1992).
- [79] V. A. Dzuba, V. V. Flambaum, and O. P. Sushkov, Phys. Rev. A **51**, 3454 (1995).

- [80] W. R. Johnson, Z. W. Liu, and J. Sapirstein, *At. Data Nucl. Data Tables* **64**, 279 (1996).
- [81] C. E. Theodosiou, *Phys. Rev. A* **30**, 2881 (1984).
- [82] M. Safronova, personal communication.
- [83] D. Sheng, personal communication.
- [84] L. Isenhower, W. Williams, A. Dally, and M. Saffman, arXiv:0901.2549v1 (2009).
- [85] J. Hood, personal communication.
- [86] Proposal submitted to the D.O.E..
- [87] G. Saathoff, H. Buhr, L. A. Carlson, A. Wolf, D. Schalm, S. Karpuk, C. Novotny, G. Huber, M. Zimmerman, R. Holzwart, T. Udem, T. W. Hansch, and G. Gwinner, *Nature Physics* **3**, 861 (2007).
- [88] *High-resolution Laser Spectroscopy*, Vol. 13 of *Topics in Applied Physics*, edited by K. Shimoda (Springer-Verlag, Berlin, 1976).
- [89] W. Demtröder, *Laser Spectroscopy* (Springer-Verlag, New York, 1996).
- [90] F. E. Becerra, R. T. Willis, S. L. Rolston, and L. A. Orozco, arXiv:0901.2960v1 (2009).
- [91] D. V. Sheludko, S. C. Bell, R. Anderson, C. S. Hofman, E. J. D. Vredenbregt, and R. E. Scholten, *Phys. Rev. A* **77**, 033401 (2008).
- [92] W.-K. Lee, H. S. Moon, and H. S. Suh, *Opt. Lett.* **32**, 2810 (2007).
- [93] V. Wong, R. S. Bennink, A. Marino, R. W. Boyd, and C. R. Stroud Jr., *Phys. Rev. A* **70**, 053811 (2004).